

POLYTECHNIC OF TURIN

Master's Degree in Mechanical Engineering

Master Thesis

Hydrostatic bearings design and test for centerless grinding machines



Thesis advisors:

Prof. Federico COLOMBO

Prof. Terenziano RAPARELLI

Company advisor:

Eng. Eugenio BOGGIO SELLA

Applicant:

Ferdinando FARACI

April 2021

Table of contents

Usual meaning of symbols	4
List of figures	6
List of tables	8
Aim of the research	9
Introduction	10
1. Bearing design	12
1.1 Known data	12
1.2 Bearing Pad	13
1.3 Bearing Pad Equivalent Area	14
1.4 Lubricant characteristics and minimum film thickness	15
1.5 Electrical analogy	16
1.5.1 Inflow resistance	17
1.5.2 Outflow resistance	17
1.6 Pressure	18
1.7 Flow	20
1.8 Bearing load capacity	21
1.8.1 Bearing load capacity calculation example	26
1.9 Bearing film thickness	27
1.10 Bearing film stiffness	29
1.11 Bearing damping	35
2. FEM Analysis	39
2.1 Problem presentation	39
2.2 Analysis	42
3. Stiffness measurement setup	46
3.1 Experimental setup	46
3.1.1 Magnet Loader	47
3.1.2 External force evaluation	50
3.1.3 V-I (Voltage to Current) Converter	54
3.1.4 Displacement measurement	57
4. Arrangement and experimental results	58
4.1 Preparation	58
4.1.1 Elements of the system	58
4.1.2 Getting ready	65
4.2 Results	69

4.2.1	Design film thickness 30 microns	70
4.2.2	Design film thickness 15 microns	75
4.3	Results overview	80
Conclusions		83
Appendix A		86
Appendix B		86
Appendix C		89
Bibliography		91

Usual meaning of symbols

Symbol	Units	Description
A_v	mm^2	Effective pad area
B	mm	Bearing pad width
C_{sq}	$\text{Ns}/\mu\text{m}$	Squeeze damping
C_x	mm	Pad land width
C_y		
d_c	mm	Capillary Tube Diameter
D_m	mm	Spindle diameter
H	mm	Recess depth
h	μm	Lubricant film thickness
h_d	μm	Design film thickness
k_i	$\text{N}/\mu\text{m}$	i th bearing pad stiffness
k_d	$\text{N}/\mu\text{m}$	Bearing pad design stiffness
k_{tot}	$\text{N}/\mu\text{m}$	Bearing stiffness
L	mm	Bearing pad length
l_c	mm	Capillary Tube Length
N	rpm	Spindle Angular velocity
P_a	Pa	Ambient Pressure
P_r	Pa	Recess Pressure
P_s	Pa	Supply Pressure
q	cm^3/s	Total flow
q_b	cm^3/s	Bearing Flow
q_i	cm^3/s	i th pad bearing flow
q_r	cm^3/s	Restrictor Flow
R_i	kg/sm^4	Inflow Resistance
R_m	mm	Spindle radius
R_o	kg/sm^4	Outflow Resistance
r_p	mm	Internal pad radius
T	$^{\circ}\text{C}$	Lubricant temperature
u_0	mm	Displacement set
W_d	N	Design load capacity
$W_{c_i}^{(h)}$	N	Central i th pad area horizontal load capacity
$W_{c_i}^{(v)}$	N	Central i th pad area vertical load capacity
$W_{l_i}^{(h)}$	N	Lateral i th lands horizontal load capacity
$W_{l_i}^{(v)}$	N	Lateral i th lands vertical load capacity
$W_i^{(h)}$	N	i th pad horizontal load capacity
$W_i^{(v)}$	N	i th pad vertical load capacity

W_h	N	Bearing horizontal load capacity
W_v	N	Bearing vertical load capacity
W	N	Bearing load capacity
$y(t)$	mm	Step response

β		P_r/P_s Pressure Ratio ($h=h_d$)
δ	μm	Spindle Displacement Module
ω	rad/s	Spindle Angular velocity
ξ		Damping ratio

List of figures

Figure 1. Journal bearing with rectangular pad and capillary restrictor. _____	11
Figure 2. Representation of the journal bearing under study with 3 bearing pads. _____	12
Figure 3. Bearing pad geometry. _____	14
Figure 4. Pressure distribution on the pad (left) and electrical analogy (right). _____	17
Figure 5. Pressure distribution on the bearing pad. _____	19
Figure 6. Oil inflow on a bearing pad with capillary restrictor ($m=q/\rho$). _____	20
Figure 7. Bearing pad divided in different areas and correspondent applied load. _____	24
Figure 8. Geometry of the journal bearing. _____	25
Figure 9. Film thickness parameters for calculation in case of displacement. _____	28
Figure 10. Influence of design load W_d and χ on the stiffness behavior of a single pad in function of the variation of design film thickness. The product between χ and load gives the stiffness behavior on film thickness variation. _____	31
Figure 11. Pad and Bearing Stiffness in function of film thickness for no spindle displacement. Numerical results referring to $l_c=500$ mm; $d_c= 1$ mm; $P_s=50$ bar; $C=21,83$ mm. _____	32
Figure 12. Stiffness comparison of different film thickness systems for pad land width variations. _____	33
Figure 13. Stiffness and recess pressure dependence to the capillary restrictor length l_c . Results referring to _____	34
Figure 14. Journal bearing stiffness referring to the vertical axes in case of spindle displacement. _____	35
Figure 15. Journal bearing stiffness referring to the vertical axes in case of spindle displacement. _____	36
Figure 16. Spindle displacement step response. _____	38
Figure 17. Support of hydrostatic bearing pad. _____	39
Figure 18. Representation of the main parameters to control the pad deflection. _____	40
Figure 19. External side of the bigger bearing pad. _____	41
Figure 20. Internal side of the bigger bearing pad. _____	41
Figure 21. Capillary tube. _____	41
Figure 22. Assembled hydrostatic bearing pad. _____	42
Figure 23. System constrains and pressure force distribution. _____	43
Figure 24. Mesh of the hydrostatic bearing pad. _____	44
Figure 25. Smaller bearing pad deflection analysis. _____	45
Figure 26. Bigger bearing pad deflection analysis. _____	45
Figure 27. Block diagram of the experimental setup. _____	46
Figure 28. U-shape magnet loader. _____	48
Figure 29. Magnet loader (electromagnet) with 450 coils. _____	50
Figure 30. External load generator. _____	51
Figure 31. Generator and measuring system of external loads. _____	52
Figure 32. Digital feeler gauger with millesimal resolution used to calculate the plate arrow. _____	54
Figure 33. Simplified V-I converter circuit schematic. _____	55
Figure 34. Homemade Texas Instrument V-I amplifier PCB. _____	55
Figure 35. Adjustable power supply used in laboratory. _____	56
Figure 36. Micrometric dial indicator device. _____	57
Figure 37. Small bearing pads. _____	59
Figure 38. Big bearing pads. _____	59
Figure 39. Regulation struts. _____	60
Figure 40. Cases and metal plate before burnishing operation. _____	60
Figure 41. Drilled screws to allow O-ring crushing. _____	61
Figure 42. Pipes and stopper preassembly. _____	61
Figure 43. Assembly of the stopper into the case. _____	62
Figure 44. Struts mounted inside the case. _____	62
Figure 45. Bushings assembled inside the case. _____	63
Figure 46. Assembled hydrostatic journal bearing. _____	63
Figure 47. Detail of the assembled machinery. _____	64
Figure 48. Experimental setup, including the measuring system. _____	64
Figure 49. Relation between current in the coils and electromagnetic force generated by the magnet loader. _____	65

Figure 50. Spindle displacement characteristics for each bearing. $P_s = 50$ bar, $h_d=30 \mu\text{m}$.	66
Figure 51. Stiffness characteristics for each bearing. $P_s = 50$ bar, $h_d=30 \mu\text{m}$.	66
Figure 52. Spindle displacement characteristics of the system. $P_s = 50$ bar.	67
Figure 53. Stiffness characteristics of the system. $P_s = 50$ bar.	67
Figure 54. Spindle arrow compensation.	68
Figure 55. Hydrostatic spindle force-displacement relation between experimental and theoretical behavior. $P_s= 30$ bar, $h_d = 30 \mu\text{m}$.	70
Figure 56. Hydrostatic spindle stiffness-displacement relation between experimental and theoretical behavior. $P_s= 30$ bar, $h_d = 30 \mu\text{m}$.	71
Figure 57. Hydrostatic spindle force-displacement relation between experimental and theoretical behavior. $P_s= 40$ bar, $h_d = 30 \mu\text{m}$.	72
Figure 58. Hydrostatic spindle stiffness-displacement relation between experimental and theoretical behavior. $P_s= 40$ bar, $h_d = 30 \mu\text{m}$.	72
Figure 59. Hydrostatic spindle force-displacement relation between experimental and theoretical behavior. $P_s= 50$ bar, $h_d = 30 \mu\text{m}$.	73
Figure 60. Hydrostatic spindle stiffness-displacement relation between experimental and theoretical behavior. $P_s= 50$ bar, $h_d = 30 \mu\text{m}$.	74
Figure 61. Hydrostatic spindle force-displacement relation between experimental and theoretical behavior. $P_s= 30$ bar, $h_d = 15\mu\text{m}$.	76
Figure 62. Hydrostatic spindle stiffness-displacement relation between experimental and theoretical behavior. $P_s= 30$ bar, $h_d = 15\mu\text{m}$.	76
Figure 63. Hydrostatic spindle force-displacement relation between experimental and theoretical behavior. $P_s= 40$ bar, $h_d = 15\mu\text{m}$.	77
Figure 64. Hydrostatic spindle stiffness-displacement relation between experimental and theoretical behavior. $P_s= 40$ bar, $h_d = 15\mu\text{m}$.	78
Figure 65. Hydrostatic spindle force-displacement relation between experimental and theoretical behavior. $P_s= 50$ bar, $h_d = 15\mu\text{m}$.	78
Figure 66. Hydrostatic spindle stiffness-displacement relation between experimental and theoretical behavior. $P_s= 50$ bar, $h_d = 15\mu\text{m}$.	79
Figure 67. Stiffness comparison of the system between three different pressure with oil gap of 30 microns.	80
Figure 68. Comparison of load characteristic by varying the clearance of the system. $P_s = 30$ bar.	81
Figure 69. Comparison of load characteristic by varying the clearance of the system. $P_s = 40$ bar.	82
Figure 70. Step 1 – Putting the bushing on the engineering blue on the spindle.	89
Figure 71. Step 2 – Evaluation of blue points and getting ready to scrape them.	89
Figure 72. Step 3 - Scraping process.	90
Figure 73. Final result of scraped pads.	90

List of tables

Table 1. Known spindle data. _____	13
Table 2. Bearing pad geometrical data. _____	15
Table 3. Mobil Velocité N°6 lubricant characteristics. _____	15
Table 4. Minimum film thickness h_{min} . _____	16
Table 5. Electrical analogy numerical results. _____	18
Table 6. Pressure on hydrostatic journal bearing. _____	19
Table 7. Lubricant flow numerical results. _____	20
Table 8. Numerical results of load in each pad. _____	25
Table 9. Bearing pad geometry for the load calculus example. _____	26
Table 10. Load capacity numerical results of the system referring to a 10 μ m displacement vertically oriented to the $\pi/2$ direction. _____	27
Table 11. Journal bearing film thickness. _____	29
Table 12. Film stiffness numerical results ($h_d=0,03$ mm; $d_c= 1$ mm; $l_c= 500$ mm; $P_s=50$ bar; $C=21,83$ mm). _____	35
Table 13. Main parameters to calculate the squeeze damping. _____	36
Table 14. Main parameters to calculate the squeeze damping. _____	37
Table 15. Pad deflection variation in relation to figure 18 parameters. _____	40
Table 16. "EN-GJMW-350-4" mechanical proprieties (related to 20 °C). _____	43
Table 17. Parameter of the electromagnet. _____	47
Table 18. Theoretical Force-Current relation. _____	48
Table 19. Relation between current on coils and plate arrow. The force is deducted through the plate stiffness. _____	52
Table 20. V-I Converter technical specification. _____	56
Table 21. Designed parameters for the two kind of bearing pads. _____	86
Table 22. Mitutoya micrometric feeler gauger datasheet. _____	86
Table 23. Correlation between current, electromagnetic force, spindle displacement and stiffness for the system with 30 microns oil film thickness for a pressure supply of 30, 40 and 50 bar. _____	87
Table 24. Correlation between current, electromagnetic force, spindle displacement and stiffness for the system with 15 microns oil film thickness for a pressure supply of 30, 40 and 50 bar. _____	88

Aim of the research

The following thesis is based on the design and development of a hydrostatic journal bearing, commonly used for high precision machinery. The work is carried out in collaboration with the company "Bocca & Malandrone S.r.l." which proposed the project, in fact the company works with machines with an accurate precision that allow to realize grinding operations.

Until today the company has realized machinery that works in the hydrodynamic field and being that high rotational speed of the machinery cannot be reached, the hydrodynamic machines do not work at their best.

Best performances are offered by a hydrostatic system, where rotational speed can even be zero to obtain good results. Hydrostatic journal bearing is the main theme of this work and the study of this system will be shown.

This thesis presents step by step how the realization of a hydrostatic journal bearing was made. It includes the design of the geometry, the fluid and pressure supply choice, the calculation of flow and forces. Moreover, an analysis of the bearing pads deflection was made.

The design of the bearing was influenced by the presence of external loads and this involved the choice of the right stiffness the bearing must have.

The hydrostatic bearing designed in the first part of the work, has not to be intended as the final bearing used in our application but it is just a generic example used for the design process.

By the way, our project is characterized by two different size hydrostatic bearing, according with the existing machine elements.

After showing the design process and the relative calculation examples, the parameters related to the two real hydrostatic bearings will be shared. It is possible to see them in the Appendix A.

The design, the realization, and the test of the system are the main section of the following work. To test how the system works under different conditions, a measuring test was created. Through it, it is possible to calculate the load and stiffness characteristic of the journal bearing.

Introduction

Hydrostatic bearings have been used for many years to provide precision and long life in machine tools and industrial machines [5].

Unlike a traditional rolling bearing, in a hydrostatic bearing the surfaces are separated by a film of oil forced between them under pressure. The liquid flows between the spindle and cylindrical metal plates and it balances the stability of the system. The pressure is generated by an external pump. Because the pressurized film is not produced by relative motion of the bearing surfaces, a complete film is present whenever the bearing is pressurized, even at zero speed [2].

Our application is about recessed hydrostatic journal bearing, where recessed refers to a part of the bearing pad where the pressure is maintained constant and journal bearing is essentially referred to a shaft which rotates inside a supporting shell. Figure 1 shows the journal bearing structure.

Lubricant at a constant supply pressure P_s is pumped towards the bearing. The pressurized lubricant first passes through the capillary restrictor where dissipation of pressure energy causes reduced pressure on entry into the recess of the bearing pad.

The recess is relatively deep compared with the bearing film thickness so that it offers little resistance to flow. Pressure in the recess is therefore constant throughout the recess volume. The flow passing through the recess leaves through the thin gap between the bearing land and the opposing surface. The pressure in the bearing film reduces as it passes across the bearing land and reaches ambient pressure, over the pad.

The film pressures oppose the applied load and maintain the separation of the surfaces. Recess pressure must be lower than supply pressure to allow for load variations. This is because the recess pressure must be able to vary with applied load variations [4].

The application of an external load let the shaft displace and it cause a reduction of the film thickness in the verse of the applied load. The local pressure proportionally increases, and a reaction force is generated. The bearing force allows, within the limits, the system to react to external loads.

The load capacity is calculated from the pressure in the bearing as shown in chapter 1.8 "*Bearing Load Capacity*".

The journal bearing under analysis does not consists of just a single cylinder of material, but it is divided in different pieces called *bushing*, in according with the number of the pads. In this thesis work is firstly analyzed a journal bearing with bushings to show the calculous process and design. Later the process is applied to the journal bearing used in our application. It consists of three, equally distanced bearing pads.

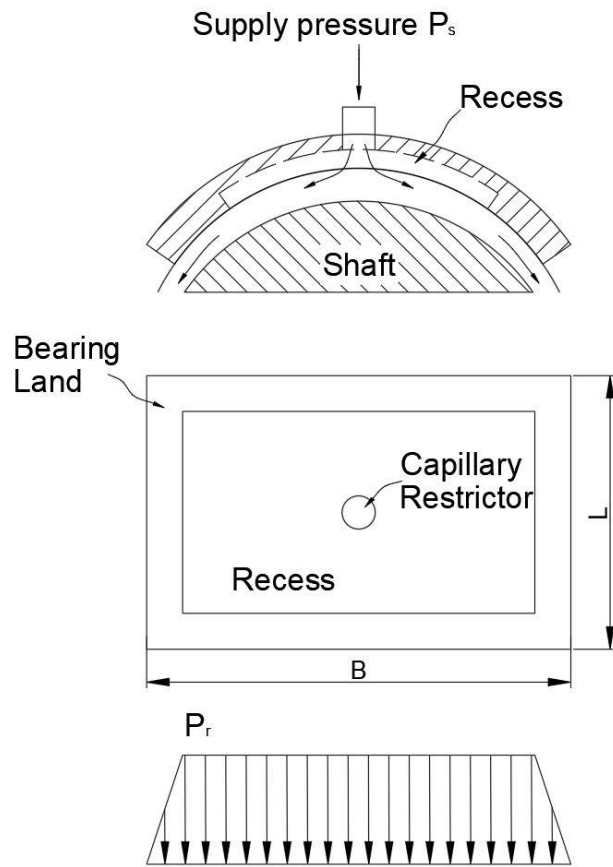


Figure 1. Journal bearing with rectangular pad and capillary restrictor.

1. Bearing design

In this study one pad is analyzed and because of the identical shape and characteristics of the others, the obtained results can be applied to the others pad. In the journal bearing with two pads, the pads are symmetrically centered on the vertical direction and the bearing can react good only to vertical external loads, making the system worthless for any kind of situations.

A journal bearing with three equally spaced pads allow the system to react good to any external load directions and it represent an affordable solution for our application.

The pad configuration chosen in this application is a recess-type configuration, figure 2.

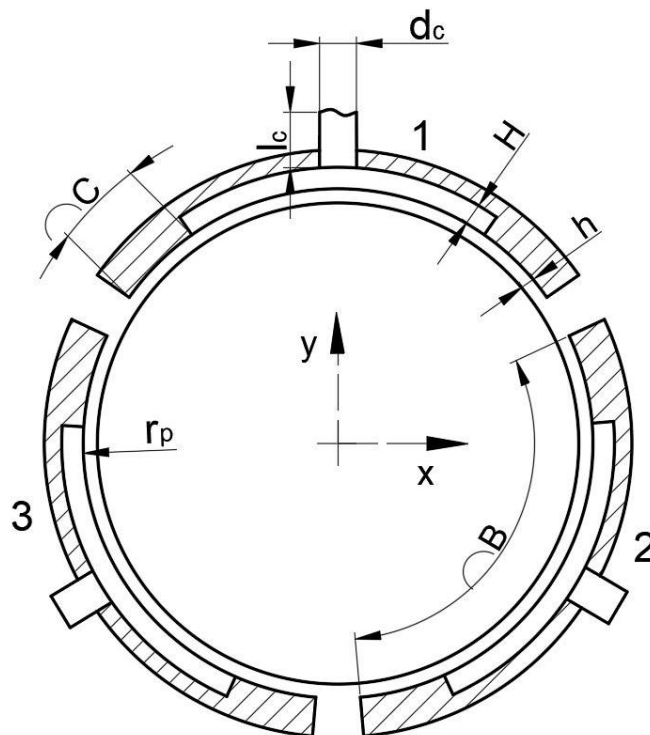


Figure 2. Representation of the journal bearing under study with 3 bearing pads.

1.1 Known data

The design of the hydrostatic bearing can be done through the knowledge of the system in which it will be applied. Knowing that the journal bearing need to support a shaft employed to grinding operation, what we need to know is the geometry of the spindle and its operating conditions.

Plus, thanks to the presence of others grinding machinery inside the company, the bearing design was made knowing the dimension of the spindle that will be used for the application.

Table 1 shows all of the initial design information that will be used in the project.

Table 1. Known spindle data.

Spindle Diameter	D_m	100	mm
Spindle Radius	R_m	50	mm
Pad Length	L	100	mm
Velocity Spindle Rotation	ω_s	300	rpm

1.2 Bearing Pad

The bearing pad is the main part of a hydrostatic bearing. It is typically realized in bronze or iron material and the presence of a capillary restrictor on it allows the lubricant to pass through the pad and to balance the whole system. The design of the bearing pad is crucial, the geometry would avoid having back-pressure to the restrictor.

Besides restrictor, the right pad geometry must be designed. The total pad area is function of the load the bearing can support. Knowing the external load, a geometry that avoid the contact between the pad and the spindle must be projected.

Knowing that the shaft is a circular element, the same will be for the bearing pads. Their geometry is circular, and each pad occupies an arc of the total shaft circumference. The internal pad radius is bigger than the shaft and its radius is due by the sum of the shaft radius and the film thickness.

Considering a journal bearing with three pads, each pad occupies a portion of 110° around the spindle. With this information it is possible to calculate the bearing pad width in the following way:

$$B = r_p * 2\pi * \frac{110^\circ}{360^\circ} \quad (1)$$

The pocket is the area where the pressure is maintained constant and it has a constant deep H that is supposed to be fifteen times bigger than the film thickness h [2], so when h will be chosen, H will be calculated by the following equation:

$$H = 15 * h \quad (2)$$

The vertical and horizontal bearing land have the same dimension and for simplicity each bearing land will be called C . An optimum land-length ratio C/L for a journal bearing pad is approximately 0,25 [4]. An appropriate valor of C will be chosen later in function of the required stiffness.

As regards the geometry of the capillary restrictor, the ratio l_c/d_c should, if possible, be greater than 100 [4], where l_c is the capillary length and d_c is the diameter of the capillary restrictor. The dimension will be chosen in function of the desired load and stiffness.

By the end of the next subchapter, all geometrical data just discussed are reported in table 2.

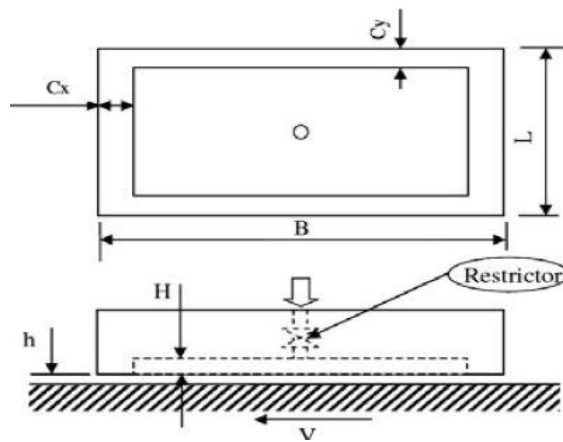


Figure 3. Bearing pad geometry.

1.3 Bearing Pad Equivalent Area

The reacting force we want the bearing to have is function of the oil pressure between the pad and the shaft and it is function of the pad geometry, particularly it depends on the bearing equivalent area of each pad. Based on the determined area is possible to calculate the effective load the bearing can support.

The bearing pad has a circular profile but for simplicity it can be considered as an opened semicircle that can be translated in a rectangular profile. This does not influence at all the application.

The effective area that allows to generate a reaction force is calculated by the following equation [1]:

$$A_v = BL - LC - BC \quad (3)$$

Table 2. Bearing pad geometrical data.

Length	L	100,00	mm
Width	B	96,05	mm
Land Width	C _x	21,83	mm
	C _y	21,83	mm
Recess Depth	H	0,45	mm
Internal Pad Radius	r _p	50,03	mm
Effective Area Equation	A _v	5325,34	mm ²
Occupied Arc by the Pad		110	°
		1,920	rad

1.4 Lubricant characteristics and minimum film thickness

Lubricant is the mean that allow the hydrostatic bearing to perform, and it ensure a friction reduction between two surfaces in relative motion.

The choice of the right lubricant is very important because its characteristics are strictly related with almost all other parameters of the journal bearing. Plus, it is fundamental to avoid the risk of seizure through the right choice.

For this application, the oil “Mobil Velociteé N°6” – ISO VG 10 was chosen. The main characteristics of the fluid are given by *Mobil™* company and are showed on table 3.

Table 3. Mobil Velociteé N°6 lubricant characteristics.

Temperature T [°C]	Cinematic Viscosity [cSt]	Density ρ [kg/m3]	Dynamic Viscosity μ [cP]
20	20,7	841,3	17,41
40	10	830,7	8,31
100	2,62	800,5	2,1

For reference we are going to take in count the fluid characteristics referring to $T = 20^{\circ}C$. The main data we will use for the study are the density and the dynamic viscosity. It is possible to convert dynamic viscosity unit to SI of Units and just dividing cP for 1000 we obtain $\mu = 0,01741 Ns/m^2$.

As regard the minimum film thickness h_{min} , it is function of the shaft diameter and rotation velocity. For our application, the minimum film thickness the lubricant must have, in according with table 4, is $7\mu m$.

Table 4. Minimum film thickness h_{min} .

Shaft diameter (mm)		Sliding speed of shaft (m/s)				
Over		-	1	3	10	30
	Up to	1	3	10	30	-
24	63	3	4	5	7	10
63	160	4	5	7	9	12
160	400	6	7	9	11	14
400	1000	8	9	11	13	16
1000	2500	10	12	14	16	18

1.5 Electrical analogy

To find the load bearing performances of a hydrostatic bearing, the system can be modeled as a fluid resistance network. The raised lands and the capillary restrictors represent resistors while the deeper grooves represent nodes where the pressure is roughly equal for the purpose of the analysis. Once the system has been modeled as a resistance network, Kirchhoff's Current Law and Kirchhoff's Voltage Law can be employed to solve the network [3].

Each bearing pad is supplied by oil in pressure through a capillary tube in the center of the pad. The fluid pass through the restrictor and the pad geometry allows to have a constant pressure in the pocket. Then the fluid is lead towards the environment through the tiny space between the pad and the shaft.

A pump at a pressure supply P_s , send the lubricant to the system. The fluid meet the first resistance R_i defined by the restrictor which resistance does not vary in time. The pressure on the pocket decreases to P_r . The fluid flows between the spindle and the pad and then is pushed out of the bearing to the environment. The thickness between the shaft and the pad can be modeled as another resistance R_o , this time variable.

Figure 4 shows both the pressure distribution on the pad and the electrical analogy used to model each one.

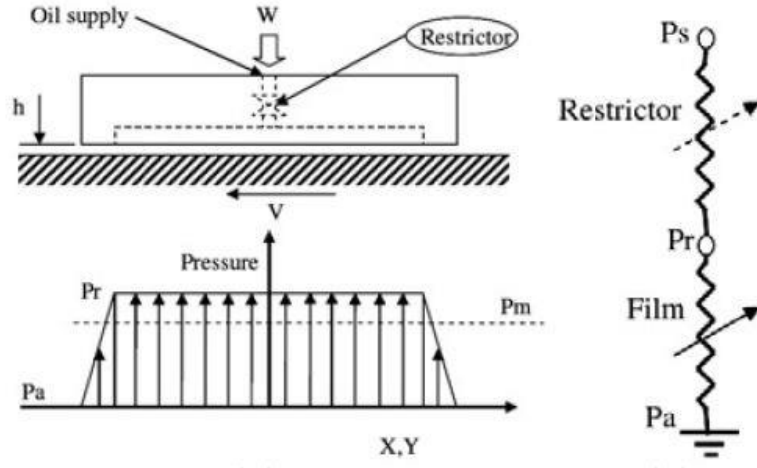


Figure 4. Pressure distribution on the pad (left) and electrical analogy (right).

1.5.1 Inflow resistance

The inflow resistance refers to the capillary restrictor. The main parameters that influence the resistance variations are the geometry of the tube and the fluid characteristics.

For a capillary restrictor, the equation to calculate the resistance through the electrical analogy is showed in the following equation[1], where, as mentioned before, the ratio l_c/d_c should be greater than 100.

$$R_i = \frac{128 l_c * \mu}{\pi * d_c^4} \quad (4)$$

1.5.2 Outflow resistance

The space between the plate and the spindle is filled by the fluid in pressured and it is generally tens of microns. The oil flows in this space and the resistance is mainly related to the thickness of the fluid. The resistance is proportional to the dynamic viscosity of the fluid and it is inversely proportional to the pad length and width and to the cube of the fluid thickness. For this reason, the spindle displacement influences the variation of the outflow resistance.

Outflow resistance is basically the viscous flow resistance over the peripheral land of the bearing [1]. The formula to calculate the resistance is expressed by the following equation (5):

$$R_o = \frac{6\mu}{h^3 \left(\frac{L}{c} + \frac{B}{c} - 3 \right)} \quad (5)$$

The following table 5 shows all numerical results obtained through using electrical analogy and they are referred to the situation of no-external-load so when there is not any spindle displacement. It is important to remember that l_c and d_c are design parameters.

Table 5. Electrical analogy numerical results.

Capillary Tube Length	l_c	500	mm
Capillary Tube Diameter	d_c	1	mm
Inflow Resistance (Capillary Restrictor)	R_i	0,35	kg/smm ⁴
Outflow Resistance Pad 1	R_{o1}	0,47	kg/smm ⁴
Outflow Resistance Pad 2	R_{o2}	0,47	kg/smm ⁴
Outflow Resistance Pad 3	R_{o3}	0,47	kg/smm ⁴

1.6 Pressure

The supply pressure P_s is maintained constant through a valve and this allow to do not let the system go away from the design conditions.

The pressure has a very important role in hydrostatic bearings. The design of the right pressure is crucial because it allow to react to external loads, so by knowing external forces, seizure can be avoided. P_s is chosen in function of the application and so it depends on external loads.

The recess pressure of the oil P_r depends on the supply pressure and on inflow and outflow resistances, so it is basically function of the supply pressure and film thickness [1]. The recess pressure increases when the film thickness decreases, and it decreases when the film thickness increases.

Equation (6) allows to calculate the recess constant pressure P_r inside the pocket.

$$P_r = P_s \frac{R_o}{R_o + R_i} \quad (6)$$

Because of a linear pressure decrease in the lands, the pressure forms a triangle distribution, and the average pressure can be considered the half of the recess pressure in the lands. Figure 5 shows the pressure distribution on the bearing pad.

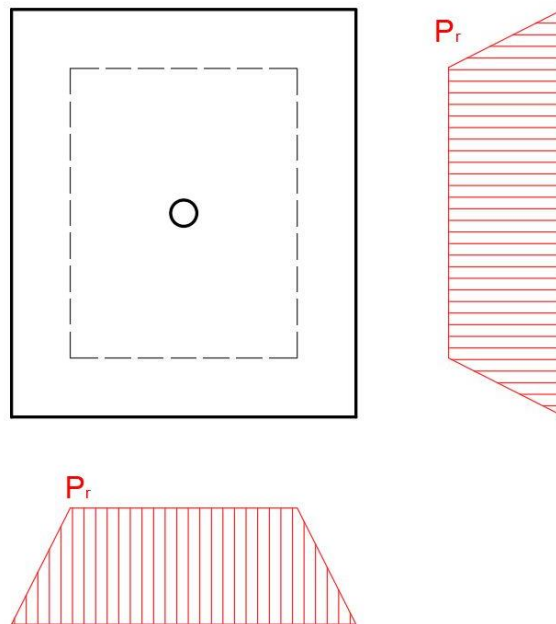


Figure 5. Pressure distribution on the bearing pad.

Table 6. Pressure on hydrostatic journal bearing.

Supply	P _s	5,00E+06	Pa
		50	bar
Precess Pocket 1	Pr1	3,23E+06	Pa
		32,29	bar
Precess Pocket 2	Pr2	3,23E+06	Pa
		32,29	bar
Precess Pocket 3	Pr3	3,23E+06	Pa
		32,29	bar
Ambient	P _a	1,01E+05	Pa
		1,01325	bar

1.7 Flow

The flow continuously varies because the space between shaft and pad is not constant when an external load is applied, so the flow increases when the film thickness increase and it decrease when the film thickness decrease, due to the variation of the resistance.

Anyway, the total flow is always constant because the flow variation in one pad is compensated by the others.

The flow can be calculated knowing the pressure and the resistance in each bearing pad. For liquid bearings, density is usually assumed to be constant so the volume flow in the restrictor and in the bearing may be equated, $q_{restrictor} = q_{bearing}$ [4]. Figure 6 illustrates the lubricant inflow inside the journal bearing and table 7 shows the numerical results obtained from the bearing design.

The flow rate through a capillary is given by Hagen-Poiseuille equation and for a laminar viscous flow we obtain the following relation (7):

$$q_r = q_b = \frac{\Delta P}{R_i + R_o} \quad (7)$$

with $\Delta P = P_s - P_a$.

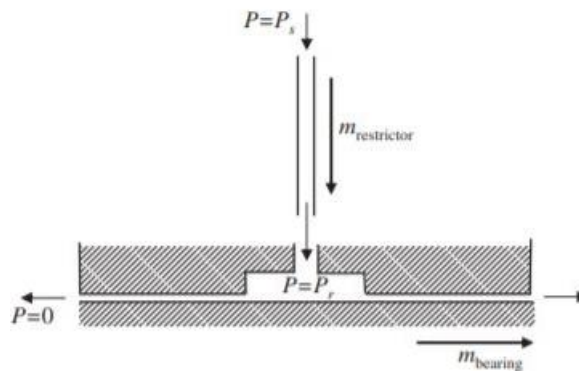


Figure 6. Oil inflow on a bearing pad with capillary restrictor ($m=q/p$).

Table 7. Lubricant flow numerical results.

Total flow	q	1,467E-05	m ³ /s
		14,673	cm ³ /s
Bearing flow	q ₁	4,89E-06	m ³ /s
		4,891	cm ³ /s
	q ₂	4,89E-06	m ³ /s
		4,891	cm ³ /s
	q ₃	4,89E-06	m ³ /s

		4,89	cm ³ /s
--	--	------	--------------------

1.8 Bearing load capacity

The force exerted by the liquid film against the two bearing members must, for equilibrium, balance the applied bearing load [2]. The bearing load capacity can be determined by multiplying the pad recess pressure for the pad effective area A_v , discussed in paragraph 1.3 “*Bearing Pad Equivalent Area*”.

A more accurate method to know the bearing load capacity is described in this chapter. It consists of a calculus through integrals that allows to take in count the different pressure distribution according to the pad geometry.

To know the total load the bearing can support, knowing that all bearing pads have the same geometry, it is possible to calculate the load capacity of one pad and then apply the same procedure to the others. To do that it is necessary to split the total pad area in different areas, according with the pressure distribution. The main area is the one with constant recess pressure P_r , then we have four lateral areas where we consider a pressure of $P_r/2$ acts. For simplicity, we grouped all the areas related to the same infinitesimal angle, referring to the radial direction.

Observing the figure 7 is possible to see the areas division and the correspondent load applied on each of them. The load calculation is made by dividing the total space occupied by the pad in different portions, related with the θ angle. Through an integral is possible to calculate the load distribution of each portion, in function of the subtended angle.

For each bearing pad the vertical and horizontal forces are calculated. The module and verse forces depend on the pad position. For example, the pad centered in $\pi/2$ does not have any horizontal force and all the load capacity is vertically oriented. The same cannot be said for a pad centered in $7/6\pi$, for example. It will have a vertical and horizontal force component.

Due to the same pads’ geometry, in case of no-external-forces the load resultant for each pad is obviously the same.

In this chapter will be analyzed the design load capacity W_d of the single pad, referring to a no-spindle-displacement situation.

To know the total load capacity of the bearing is possible to simply sum the load capacity of each bearing pad.

Considering that we want to know the load distribution in function of the infinitesimal pad width dS , it is possible to relate the width with the angle θ and the bearing pad radius r_p through the following equation (8):

$$dS = r_p d\theta \quad (8)$$

Before calculating the total load capacity, it is opportune to calculate the bearing load capacity in the horizontal and vertical direction and then we obtain the resultant. The horizontal component is calculated through the integral of the cosine of the related angle and the vertical one through the integral of the sine of the related angle.

According with the figure 7 and figure 8, we obtain the horizontal and vertical component, respectively described with the apex (h) and (v). The following equations describe the horizontal forces:

$$W_{c_i}^{(h)} = \int_{\vartheta_1^i}^{\vartheta_2^i} P_r(L - C_y) * r_p \cos(\theta) d\theta \quad (9)$$

$$W_{L_i}^{(h)} = \frac{P_r}{2} L * r_p \left[\int_{\vartheta_0^i}^{\vartheta_1^i} \cos(\theta) d\theta + \int_{\vartheta_2^i}^{\vartheta_3^i} \cos(\theta) d\theta \right] \quad (10)$$

and the following equations describe the vertical forces:

$$W_{c_i}^{(v)} = \int_{\vartheta_1^i}^{\vartheta_2^i} P_r(L - C_y) * r_p \sin(\theta) d\theta \quad (11)$$

$$W_{L_i}^{(v)} = \frac{P_r}{2} L * r_p \left[\int_{\vartheta_0^i}^{\vartheta_1^i} \sin(\theta) d\theta + \int_{\vartheta_2^i}^{\vartheta_3^i} \sin(\theta) d\theta \right] \quad (12)$$

where $d\theta$ is the infinitesimal angle related to the radial position of the bearing pad, ϑ_0^i and ϑ_1^i are the angles that include the portion of the left lateral land ($W_{L_i(1)}$ —figure 7), ϑ_1^i and ϑ_2^i are the angle that include the central portion of the bearing pad (W_{c_i} —figure 7) and ϑ_2^i and ϑ_3^i are the angle that include the portion of the right lateral land ($W_{L_i(2)}$ —figure 7), each one referring to the i th bearing pad.

W_{L_i} is obtained by summing $W_{L_i(1)}$ and $W_{L_i(2)}$ of the figure 7.

Solving the equations(9) to (12), the finite solution is obtained. It is showed through the following equations (9)', (10)',(11)' and (12)'.

$$W_{c_i}^{(h)} = P_r * r_p * (L - C_y) * [\sin(\theta)]_{\vartheta_1^i}^{\vartheta_2^i} \quad (9)'$$

$$W_{L_i}^{(h)} = \frac{P_r}{2} L * r_p * \left([\sin(\theta)]_{\vartheta_0^i}^{\vartheta_1^i} + [\sin(\theta)]_{\vartheta_2^i}^{\vartheta_3^i} \right) \quad (10)'$$

$$W_{c_i}^{(v)} = P_r * r_p * (L - C_y) * [-\cos(\theta)]_{\vartheta_1^i}^{\vartheta_2^i} \quad (11)'$$

$$W_{L_i}^{(v)} = \frac{P_r}{2} L * r_p * \left([-\cos(\theta)]_{\vartheta_0^i}^{\vartheta_1^i} + [-\cos(\theta)]_{\vartheta_2^i}^{\vartheta_3^i} \right) \quad (12)'$$

After that it is possible to obtain the total load in the horizontal and vertical direction for each pad, through the summatory of the single load contribute of the pad. The following equations show the final step.

$$W_i^{(v)} = W_{L_i}^{(v)} + W_{c_i}^{(v)} \quad (13)$$

$$W_i^{(h)} = W_{L_i}^{(h)} + W_{c_i}^{(h)} \quad (14)$$

The load capacity of each pad is defined by the following equation (15):

$$W_i = \sqrt{\left(W_i^{(h)}\right)^2 + \left(W_i^{(v)}\right)^2} \quad (15)$$

Equation (15) shows the load capacity of the single pad and it will variate when a spindle displacement occurs. When the spindle is perfectly centered in the bearing, the film thickness is the same in the whole bearing and the load capacity of each pad is the same and it corresponds to the design load capacity W_d . The numerical valor is showed in the table 8 jointly to the load capacity of each pad in the case of no-external-load condition.

To know the load capacity of the whole hydrostatic bearing, it is just necessary to sum the contribute of each bearing pad and we obtain the horizontal and vertical load capacity components and through the (15) it is possible to calculate the resultant that correspond to the bearing reaction force in case of any direction of spindle displacement.

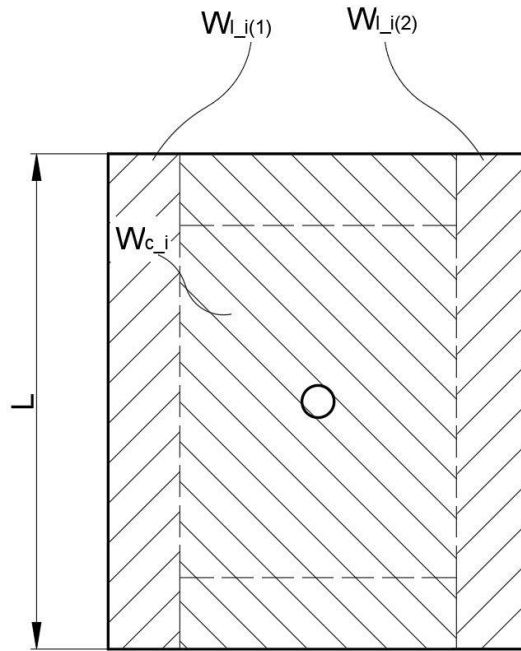


Figure 7. Bearing pad divided in different areas and correspondent applied load.

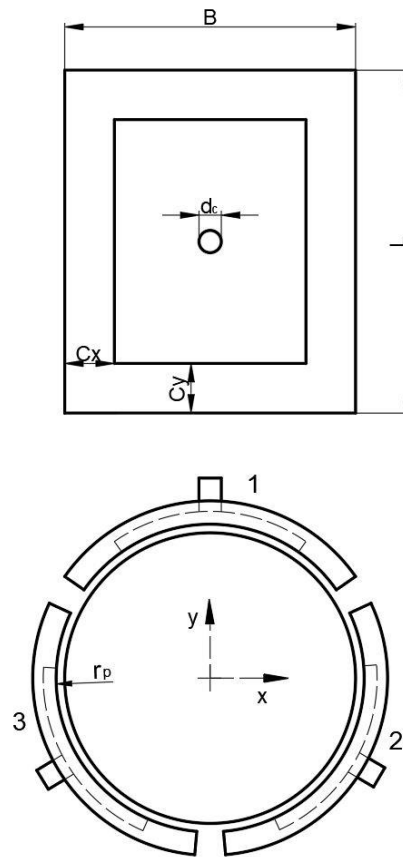


Figure 8. Geometry of the journal bearing.

Table 8. Numerical results of load in each pad.

Design load capacity			W_d	17786	N
Pad 1	Central area	Horizontal	$W_{c_1}^{(h)}$	0	N
		Vertical	$W_{c_1}^{(v)}$	12630	N
	Right and Left land	Horizontal	$W_{l_1}^{(h)}$	0	N
		Vertical	$W_{l_1}^{(v)}$	5156	N
	Horizontal Load		$W_1^{(h)}$	0	N
	Vertical Load		$W_1^{(v)}$	17786	N
	Total Load		W_1	17786	N
Pad 2	Central area	Horizontal	$W_{c_2}^{(h)}$	-10938	N
		Vertical	$W_{c_2}^{(v)}$	-6315	N
	Right and Left land	Horizontal	$W_{l_2}^{(h)}$	-4466	N
		Vertical	$W_{l_2}^{(v)}$	-2578	N
	Horizontal Load		$W_2^{(h)}$	-15403	N
	Vertical Load		$W_2^{(v)}$	-8893	N
	Total Load		W_2	17786	N
	Central area	Horizontal	$W_{c_3}^{(h)}$	10938	N

Pad 3		Vertical	$W_{c_3}^{(v)}$	-6315	N
	Right and Left land	Horizontal	$W_{l_3}^{(h)}$	4466	N
		Vertical	$W_{l_3}^{(v)}$	-2578	N
	Horizontal Load		$W_3^{(h)}$	15403	N
	Vertical Load		$W_3^{(v)}$	-8893	N
	Total Load		W_3	17786	N
TOTAL	Horizontal Load		$W^{(h)}$	0	N
	Vertical Load		$W^{(v)}$	0	N
	Total Load		W	0	N

1.8.1 Bearing load capacity calculation example

For this example, we consider a journal bearing consisting of three bearing pads equally spaced where each one occupies an arc of the circumference pair to 110° .

Being that the design load capacity calculation has just been shown, in this case we want to consider the load capacity of each pad in the case of a spindle displacement. For simplicity we consider a $10\mu\text{m}$ displacement vertically oriented to the $\pi/2$ direction. Basically, the spindle goes up and the film thickness of the pad 1 is reduced, the local pressure increases and even the load capacity grows.

The geometry of the bearing pads is showed in table 9. The land width C is related to the portion of a chosen angle pair to $25^\circ \cong 0,44 \text{ rad}$ and B is related to an angle of $60^\circ \cong 1,05 \text{ rad}$. The result in *mm* is given through equation (1).

Integrating for each portion of the pad, we obtain the load capacity in the vertical and horizontal components and then the total load given by equation (15), for each bearing pad and for the whole hydrostatic journal bearing.

If we analyze the bearing pad 1 that, according to figure 2, is centered in $\pi/2$, its horizontal (x) component of the load is null. It happens because of the pad center position that allow to have the same and opposite horizontal forces in the right and left side of the pad. The same cannot be said for the others pad because they are centered in a different position and they will always have both the horizontal and vertical component different to zero.

Table 10 shows the numerical results referring to the described situation.

Table 9. Bearing pad geometry for the load calculus example.

Length	L	100,00	mm
Width	B	96,05	mm
Land width	C	17,46	mm
Design film thickness	h	0,03	mm

Internal pad radius	r_p	50,03	mm
Arc of the circle		110	°
		1,920	rad

Table 10. Load capacity numerical results of the system referring to a $10\mu\text{m}$ displacement vertically oriented to the $\pi/2$ direction.

Pad 1	Central area	Horizontal	$W_{c_1}^{(h)}$	0	N
		Vertical	$W_{c_1}^{(v)}$	16822	N
	Right and Left land	Horizontal	$W_{l_1}^{(h)}$	0	N
		Vertical	$W_{l_1}^{(v)}$	6868	N
	Horizontal Load		$W_1^{(h)}$	0	N
	Vertical Load		$W_1^{(v)}$	23689	N
	Total Load		W_1	23689	N
Pad 2	Central area	Horizontal	$W_{c_2}^{(h)}$	-9053	N
		Vertical	$W_{c_2}^{(v)}$	-5227	N
	Right and Left land	Horizontal	$W_{l_2}^{(h)}$	-3696	N
		Vertical	$W_{l_2}^{(v)}$	-2134	N
	Horizontal Load		$W_2^{(h)}$	-12749	N
	Vertical Load		$W_2^{(v)}$	-7360	N
	Total Load		W_2	14721	N
Pad 3	Central area	Horizontal	$W_{c_3}^{(h)}$	9053	N
		Vertical	$W_{c_3}^{(v)}$	-5227	N
	Right and Left land	Horizontal	$W_{l_3}^{(h)}$	3696	N
		Vertical	$W_{l_3}^{(v)}$	-2134	N
	Horizontal Load		$W_3^{(h)}$	12749	N
	Vertical Load		$W_3^{(v)}$	-7360	N
	Total Load		W_3	14721	N
Total	Horizontal Load		$W^{(h)}$	0	N
	Vertical Load		$W^{(v)}$	8968	N
	Total Load		W	8968	N

1.9 Bearing film thickness

When projecting a journal bearing, it is very important to focus on the behavior of the oil. A right thickness must be chosen to allow an optimization of the system. Large thickness must be avoided because the bearing resistance would be lower and there would be a lost in pressure: the bearing would resist less to external loads. Too tiny thickness must be avoided too because a little

displacement of the shaft would cause a contact between the bearing plate and the spindle and for a rotating shaft, it means seizure.

Plus, the effect of external loads must be considered. When an external load is applied, a shaft displacement occurs. The reactivity of the system to restore the shaft position, depends on supply pressure, pad geometry and film thickness.

An opportune film thickness will be chosen considering different parameters linked to it. Being the project focused on a good behavior of the system depending on its load and stiffness, in relation on external forces, the film thickness h will be function of these parameters and its valor will be showed at the end of this subchapter.

Now considering that an external force can cause the spindle displacement in any direction, the film thickness variation must be linked to the module and direction of the displacement, in order to calculate the film thickness in each bearing pad.

To know the film thickness in a specific position is possible to use the following equation (16):

$$h = h_d [1 - e * \cos(\phi)] \quad (16)$$

where:

- h_d is the design film thickness of the bearing that means a no-external-load condition,
- $e = \frac{\delta}{h_d}$ with δ the module of the displacement,
- ϕ is the angle between the direction of the load and the position of the bearing pad or of the desired measuring point.

For a better understanding, all parameters involved in the equation (16) are showed in figure 9.

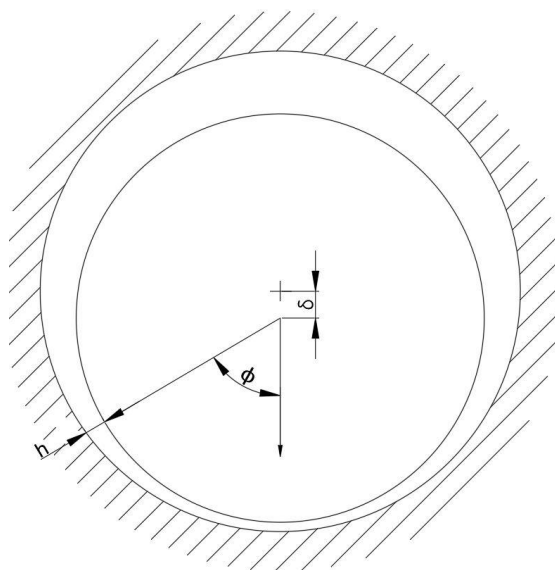


Figure 9. Film thickness parameters for calculation in case of displacement.

Table 11.Journal bearing film thickness.

Design film thickness	h_d	0,030	mm
Film thickness Pad 1	h_1	0,030	mm
Film thickness Pad 2	h_2	0,030	mm
Film thickness Pad 3	h_3	0,030	mm
Displacement	δ/h_d	e	0,00
	Module	δ	0 mm
	Direction	--	0 °

1.10 Bearing film stiffness

Hydrostatic bearing must employ a control mechanism. This is usually incorporated through the prevision of capillary restrictor. The purpose of the capillaries is to control the change in film thickness with variation in load. The rate of increase of load with deflection is termed the stiffness [6]. In terms of the bearing film thickness h , stiffness is a measure of the applied load necessary to produce a small change in lubricant film thickness and is defines as

$$k = -\frac{dW}{dh}$$

The value of stiffness for the capillary controlled bearing is maximum when the pressure ratio is $\beta = 0,5$ [6]. This will be demonstrated through figure 12.

Stiffness allows the system to react to external load and we want to maximize the stiffness to increase the reactivity of the system and the safeness conditions. It will be shown that film stiffness is related with several variables – geometrical and operatives– and it is very important to accurately define all of those.

The equation that allows to calculate the film stiffness of the i th pad k_i is the following(17):

$$k_i = 3 * \frac{W_d \xi (1 + \xi) \left(\frac{h}{h_d}\right)^2}{h_d \left(1 + \xi \frac{h^3}{h_d^3}\right)^2} \quad (17)$$

where:

- h_d is the designed film thickness, it corresponds to a no-external-load condition,

- W_d is the design load of the single pad, when $h = h_d$,
- $\xi = \frac{R_i}{R_o}$ for $h = h_d$.

Going deeper in the equation (17) it is possible to analyze the dependence of the various parameters on the film stiffness k . Expressing the equation (17) to the minimum terms, we obtain the following equation (18):

$$k_i = 3 * W_d * \frac{h^2 t (1 + t h_d^3)}{(1 + t h^3)^2} \quad (18)$$

where t is a geometric factor and it is due by $t = \frac{64}{3} \frac{l_c}{\pi * d_c^4} \left(\frac{L}{C} + \frac{B}{C} - 3 \right)$.

Now if we assume to study the stiffness in the design condition ($h = h_d$), we obtain:

$$k_i = 3 W_d * \frac{h_d^2 t (1 + t h_d^3)}{(1 + t h_d^3)^2} \quad (19)$$

The behavior of the film stiffness is goodly described by the second member of equation (19) relation $\chi = \frac{h_d^2 t (1 + t h_d^3)}{(1 + t h_d^3)^2}$. It takes in count the geometric factor and the design film thickness variation. Figure 10 is about a qualitative graph and it shows how the stiffness of the single pad is influenced by the two main terms χ and W_d , for variations of the design film thickness.

Remembering that the bearing load vary with film thickness (it increases for thickness decrease), it gives a big contribute to increase stiffness when film thickness is little. When film thickness increase, pressure decrease so even load decrease and the stiffness is reduced.

The film stiffness of the whole hydrostatic bearing k_{tot} , calculated in the vertical position is given by the following equation:

$$k_{tot} = k_1 + (k_2 + k_3) * \sin(\pi/6) \quad (20)$$

In Figure 11 is represented in detail the stiffness behavior of the figure 10 and it is showed the difference between the stiffness of the single pad and the journal bearing stiffness when the design film thickness changes.

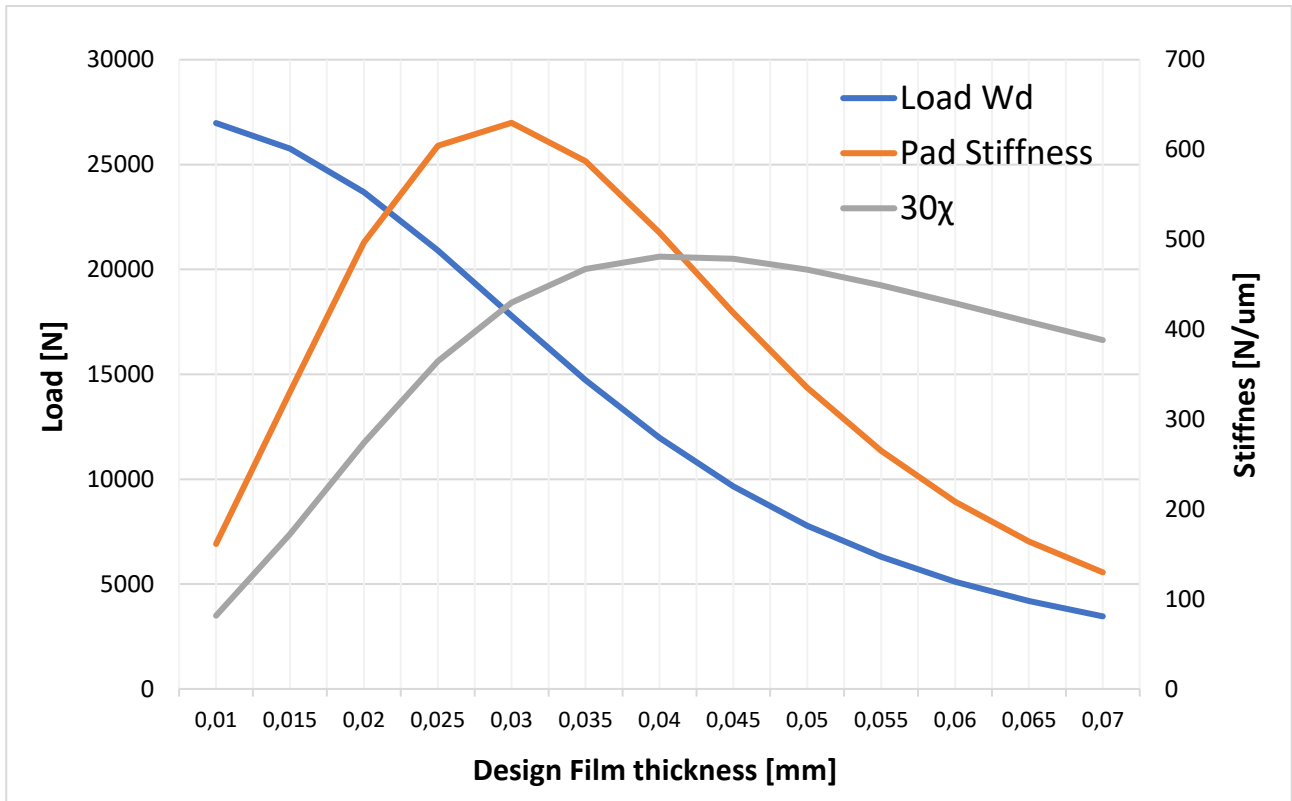


Figure 10. Influence of design load W_d and χ on the stiffness behavior of a single pad in function of the variation of design film thickness. The product between χ and load gives the stiffness behavior on film thickness variation.

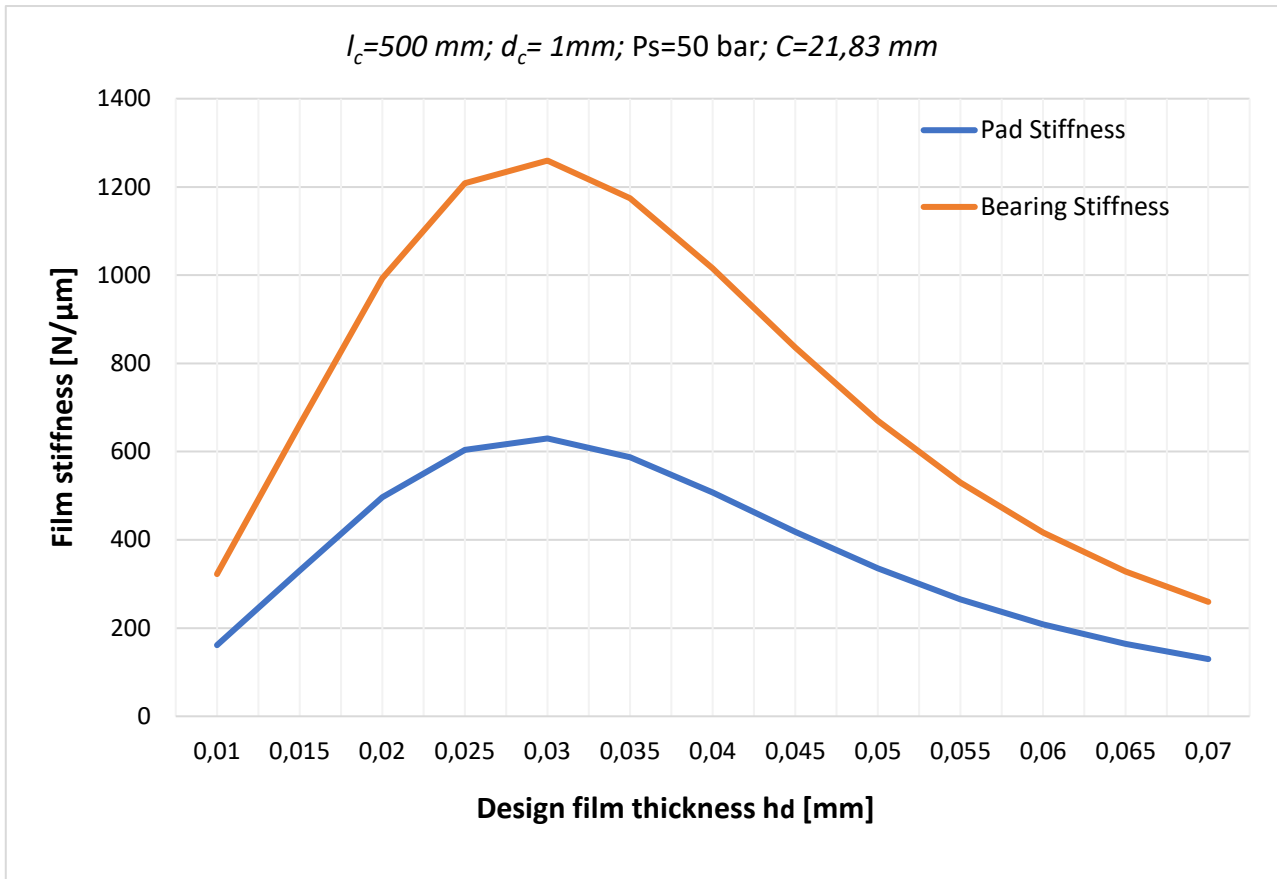


Figure 11. Pad and Bearing Stiffness in function of film thickness for no spindle displacement. Numerical results referring to $l_c=500$ mm; $d_c= 1$ mm; $P_s=50$ bar; $C=21,83$ mm.

In figure 12 is showed the behavior of the film stiffness in function of the land width C variation. Three different cases, in which the design film thickness h_d is changed, are showed. It is possible to see that for too small land widths, the stiffness strongly depends on the film thickness and the difference could even be huge (this can be seen comparing $h_d=0,02$ mm to $h_d=0,04$ mm where the stiffness difference, at the same land width dimension $C=4,4$ mm, is about 1000 $N/\mu m$). For values of C bigger than 15 mm the stiffness behavior for different film thickness is very similar.

Another aspect of the stiffness that was analyzed is related to the capillary restrictor length variation. Knowing that the film stiffness is function of the geometric factor t and knowing that t is proportional to the restrictor length l_c , an analysis was made through figure 13.

Firstly, increasing l_c , due to the increase of the geometric factor t , an increase of the stiffness occurs. After, reaching a certain value of l_c , the stiffness softly decreases. This can be explained by seeing at the pressure behavior that is all time decreasing (lost in pressure occurs by increasing the restrictor length), so the design load W_d decreases too.

The stiffness decreases because the reduction in pressure has a bigger effect than other parameters which whom it is linked to.

Another aspect important to observe is that the stiffness peak is reached when the pressure supply is the double of the pressure recess ($l_c \cong 900 \text{ mm}$), $\beta = 0,5$ — as we talked before.

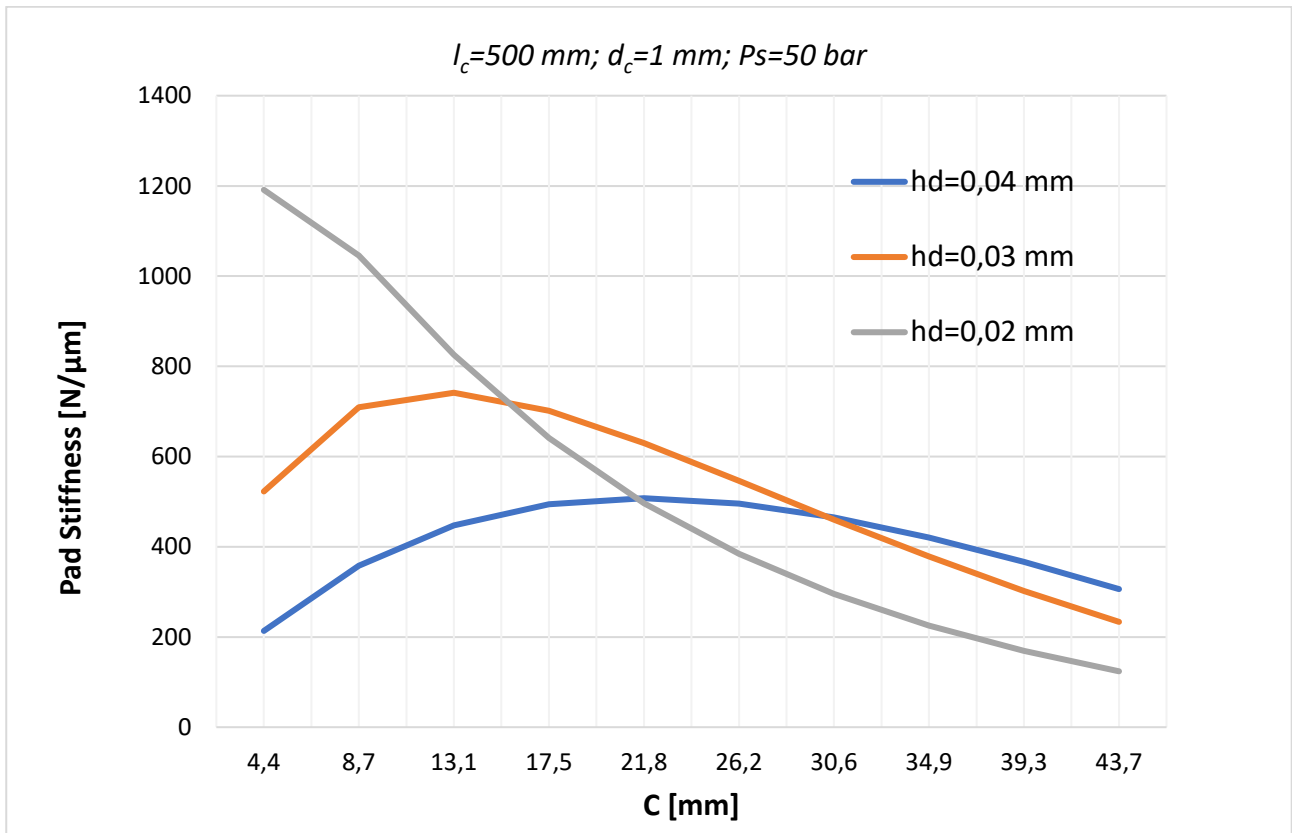


Figure 12. Stiffness comparison of different film thickness systems for pad land width variations.

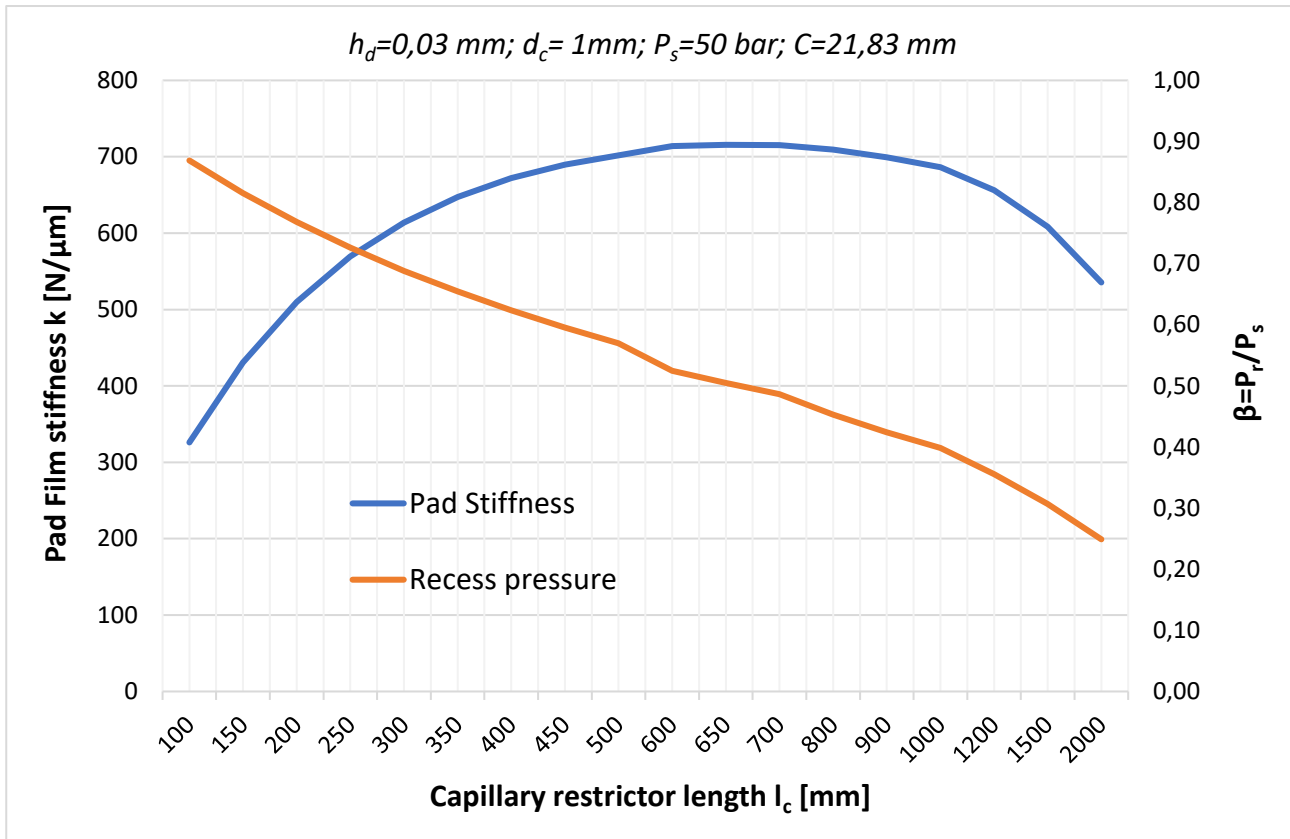


Figure 13. Stiffness and recess pressure dependence to the capillary restrictor length l_c . Results referring to $h_d=0,03$ mm; $d_c= 1$ mm; $P_s=50$ bar; $C=21,83$ mm.

An important aspect to consider is due to the spindle displacement. When this occurs, the bearing film stiffness changes. To evaluate the stiffness calculation given by the equation (17), the bearing stiffness was even calculated by dividing the force generated by the spindle displacement for the displacement itself, in the following way:

$$k = \frac{W}{\delta} \quad (21)$$

Figure 14 shows the stiffness variation (related to the vertical axes) when an external load occurs. It is shown how the film stiffness varies in function of the vertical spindle displacement. The figure is referred to an upper spindle displacement causing a reduction of the film thickness between the spindle and the pad 1. The two methods for the bearing stiffness calculation are compared. For small displacements equation (21) is preferred because it is more conservative.

Table 12 resume the numerical stiffness results for each bearing pad. The numbers are referred to a no-external-load condition.

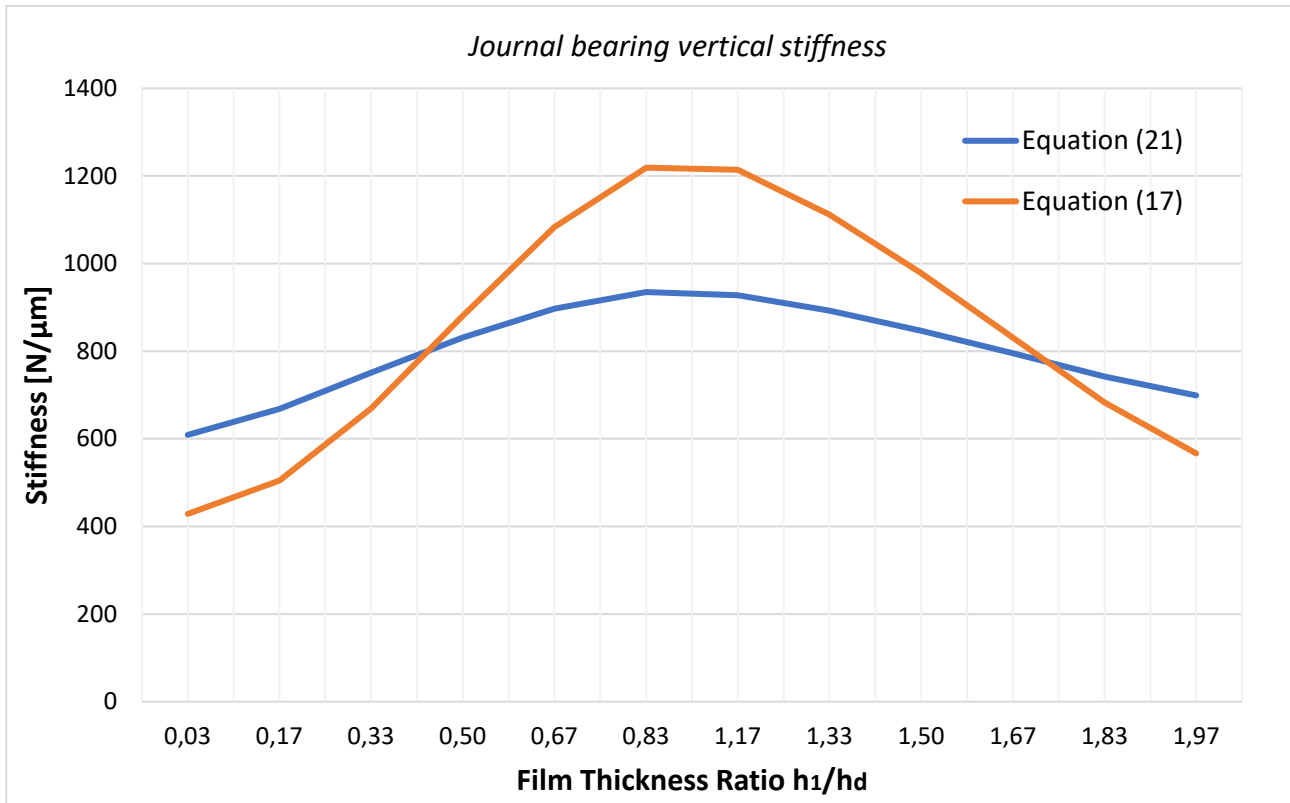


Figure 14. Journal bearing stiffness referring to the vertical axes in case of spindle displacement.

Table 12. Film stiffness numerical results ($h_d=0,03$ mm; $d_c= 1$ mm; $l_c= 500$ mm; $P_s=50$ bar; $C=21,83$ mm).

Nominal (design)	k_d	655947,73	N/mm
		655,95	N/μm
1 Stiffness Pad 1	k_1	655947,73	N/mm
		655,95	N/μm
2 Stiffness Pad 2	k_2	655947,73	N/mm
		655,95	N/μm
3 Stiffness Pad 3	k_3	655947,73	N/mm
		655,95	N/μm

1.11 Bearing damping

The dynamic behavior of a system involves the forces and vibrations of all the machine elements. The presence of a liquid film in a machine is a source of vibration damping, where the vibrations act to squeeze the liquid through the tiny channel.

The squeeze effect in a hydrostatic bearing is a well-known mechanism that operates in the same way as a hydraulic damper (Figure 15a, b). In both cases, a volume of liquid has to be displaced

at a flow rate equal to the projected area of the moving surface multiplied by the squeeze velocity V , i.e. $q_{squeeze} = A * V$ [4].

Squeeze damping C_{sq} is the main source of damping in a machine containing a hydrostatic bearing.

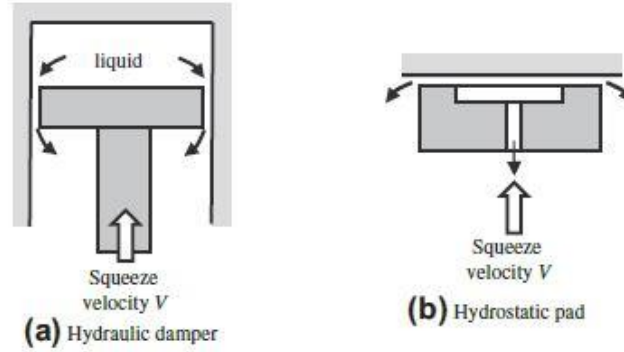


Figure 15. Journal bearing stiffness referring to the vertical axes in case of spindle displacement.

The dynamic analysis of hydrostatic and hybrid bearings is limited, in general, by insufficient reliable data. By limiting consideration to the concentric condition, $\delta = 0$, it is possible to achieve solutions. Squeeze damping is simply related to hydrodynamic stiffness according to

$$C_{sq} = \frac{\lambda_{hd}}{\pi N} \quad (22)$$

Table 13. Main parameters to calculate the squeeze damping.

$\lambda_{hs} = \frac{P_s L D}{h_0} \frac{3n^2}{2\pi} \sin^2(\pi/n) \frac{\left(1 - \frac{c}{L}\right) \beta}{Z + 1 + 2\gamma \sin^2(\pi/n)}$	Hydrostatic stiffness
$\lambda_{hd} = \frac{P_s L D}{h_d} 12n^2 \sin^2(\pi/n) S_h \frac{\left(\frac{c_x}{L}\right) \left(\frac{L}{D}\right)^2 \left(1 - \frac{c_x}{L}\right)^2}{Z + 1 + 2\gamma \sin^2(\pi/n)}$	Hydrodynamic stiffness
$Z = \beta / 1 - \beta$	Capillary factor
$\beta = \frac{P_r}{P_s} \text{ when } h = h_d$	Pressure ratio
$\gamma = n * C_x \frac{(B - C_x)}{\pi D C_y}$	Circumferential flow factor
$S_h = \frac{\mu N}{P_s} \left(\frac{D}{2h_d}\right)^2$	
$\omega_n = \sqrt{\lambda_{hs}/m}$	Natural frequency

D	Journal bearing diameter
N	Number of rotations per second
M	Spindle mass

After calculating the squeeze damping, is possible to calculate the damping ratio ζ through the following equation [4]:

$$\zeta = \frac{1}{2} \frac{C_{sq} * \omega_n}{\lambda_{hs}} \quad (23)$$

Table 14 shows the numerical results of bearing damping calculation.

Table 14. Main parameters to calculate the squeeze damping.

Mass	m	20	kg
Pressure Ratio Pr/Ps	β	0,57	
	S_h	0,05	
Capillary Factor	Z	1,33	
Circumferential Flow Factor	γ	0,75	
ω Shaft	N	300	rpm
Hydrostatic Stiffness	λ_{hs}	732,81	N/ μ m
Hydrodynamic Stiffness	λ_{hd}	204,16	N/ μ m
Damping Squeeze	C_{sq}	13,00	Ns/ μ m
Natural Frequency	ω_n	1914,16	rad/s
		304,65	Hz
Damping Ratio	ξ	16,98	

After knowing all numerical values related to the bearing damping, it is possible to calculate the reactivity of the system to come back to the design position, after a spindle displacement. If we imagine displacing the spindle of a certain value, giving a step command, the step response of the system can be calculated by the following equation [9]:

$$y(t) = gu_0 \left[1 + \frac{e^{-\omega_n t (\xi - \sqrt{\xi^2 - 1})}}{2\sqrt{\xi^2 - 1} (\sqrt{\xi^2 - 1} - \xi)} + \frac{e^{-\omega_n t (\xi + \sqrt{\xi^2 - 1})}}{2\sqrt{\xi^2 - 1} (\sqrt{\xi^2 - 1} + \xi)} \right] \quad (24)$$

where $y(t)$ represent the behavior of the spindle displacement during the time t , g is the static gain that we assume equal to 1 and u_0 is the displacement set, intended as the value we want the spindle to do.

Figure 16 shows the behavior of the spindle after giving a displacement command equal to $20 \mu\text{m}$. It is possible to see that the spindle reaches the desired position after about 70 ms and 100 ms – respectively the smaller and the bigger pad - from the input command.

It is important to underline that a similar behavior represent the situation characterized by an external force that moves the spindle from the design position to another one. In our study we want to analyze the time needed to bring back the spindle to the design position, after a force occurs. By the way, the time lag for both situations can be considered the same, as shown down.

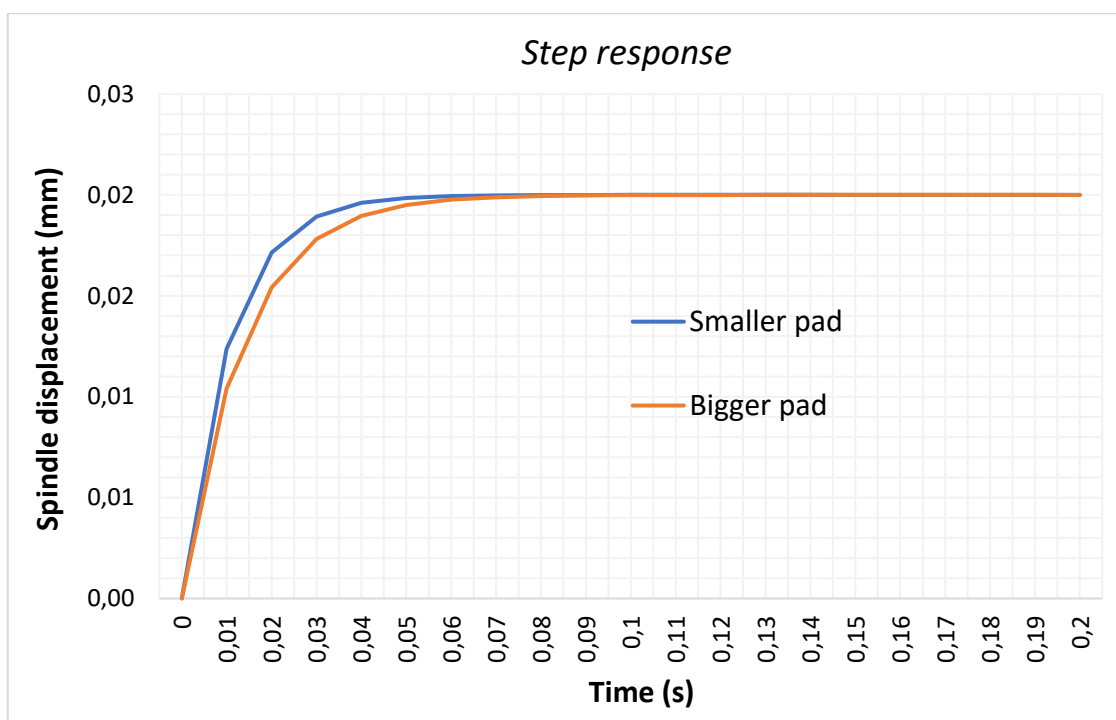


Figure 16. Spindle displacement step response.

2. FEM Analysis

2.1 Problem presentation

The dynamic characteristics of a hydrostatic bearing are not the only features to be considered. It is very important to project them to guarantee a good solidity of the mechanism, but it is even opportune to consider others relevant factors.

Being that the pads are subjected to high pressure forces, the deformation of the pad can easily occur, causing the increase of lubricant gap thickness and reducing the pressure between the spindle and the bushings, and it means a loss in rigidity and stability.

To avoid, or strongly reduce, such a phenomenon is necessary to focus on the right choose of the material, on the design of the pad thickness and on pads' width.

To analyze the deformation, the finite element method (FEM) was used. It allows to study the problem and to eventually correct the parameters, to obtain the best result possible.

Another important element to consider is characterized by the pad support, that has the role to link the pad to the carcass.

Being the carcass already been realized, the choose of the support was highly limited. The pad support consists of a circular iron element, locked on a hole of the carcass on one hand, and welded in the pad on the other hand. Figure 17 shows the support element.



Figure 17. Support of hydrostatic bearing pad.

The deformation of the pad is also strongly influenced by the amount of the support inserted into the pad. Increasing the depth j – figure 18, the pad deflection is reduced. Other parameters

showed in figure 18 were modelled in order to obtain the smaller deflection possible. The numerical values are showed in table 15 for both hydrostatic bearing.

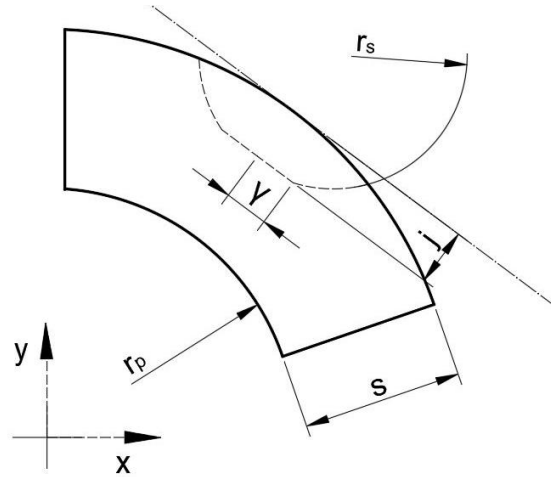


Figure 18.Representation of the main parameters to control the pad deflection.

Table 15.Pad deflection variation in relation to figure 18 parameters.

γ	[mm]			Maximum pad deflection [μm]	
	Thickness s	Support radius r _s	Support depth j	Bronze	Steel (30CrNiMo8)
5,40	18,00	15,08	7,50	12,05	6,59
5,40	18,00	15,08	9,50	10,70	5,77
5,40	21,00	15,08	7,50	9,08	5,05
5,40	21,00	15,08	9,50	8,10	4,40
5,40	21,00	15,08	10,5	7,78	4,23
5,40	18,00	16,08	7,50	11,58	6,35
6,40	18,00	16,08	7,50	11,34	6,19
6,40	18,00	16,08	9,50	9,89	5,27
6,40	21,00	16,08	9,50	7,52	4,03
6,40	21,00	16,08	7,50	8,59	4,73
6,40	18,00	15,08	7,50	11,74	6,41
7,40	18,00	15,08	7,50	11,32	6,18

To better understand the geometry of the pad, it is possible to look at the figure 19 and figure 20. It is possible to see that there is a little hole on the pad that links the lateral face of the pad with the internal one. This route allows to place the oil duct that has to role to connect the lubricant supply to the pad pocket. The capillary tube that will be inserted on the pad is showed in figure 21.



Figure 19. External side of the bigger bearing pad.



Figure 20. Internal side of the bigger bearing pad.



Figure 21. Capillary tube.

The assembled piece composed by the pad, the support and the tube, is showed in the following figure 22.

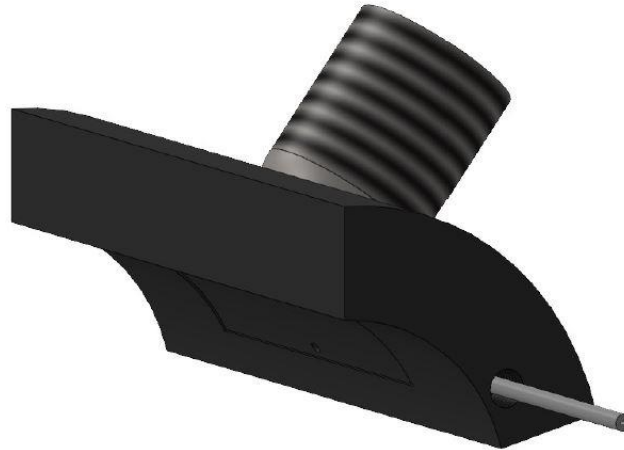


Figure 22. Assembled hydrostatic bearing pad.

2.2 Analysis

The FEM analysis was made through the software “Solidworks”. After assembling and coupling all the single elements – as shown in figure 22, the pad deflection analysis has been started.

The first step was related to the material choice. At the beginning, a bronze pad was created, and the deflection analysis was started. This analysis was compared to another one related to an iron pad. The result was that the deflection obtained with the iron pad is pair to about the half of the deflection resulting from the bronze pad.

Being that the deflection obtained with the bronze pad results of the order of the film thickness, this material was discarded. But in any case, the iron pad has the problem to facilitate the seizure effects, so even this material must be discarded.

A perfect compromise is given by the cast-iron. This material has mechanical proprieties that are interim the two described materials, so a pad with this material can guarantee a good deflection compromise and the effects of seizure are less dangerous in relation to the iron.

The hydrostatic bearing pads were realized in “EN-GJMW-350-4” (ISO JMW/350-4) malleable cast iron material and the mechanical proprieties are showed in table 15 [10].

Table 16. “EN-GJMW-350-4” mechanical proprieties (related to 20 °C).

Poisson's ratio [ν]	0,271	0,271	[-]
Elastic modulus [E]	175	195	GPa
Thermal conductivity [λ]	42	63	W/(m·K)
Specific heat capacity [c_p]	460	500	J/(kg·K)
Shear modulus [G]	64	64	GPa
Tensile strength [R_m]	270	360	MPa
Coefficient of thermal expansion [α]	0,00001	0,000014	1/K
Hardness, Brinell [HB]	230	230	[-]
Electrical resistivity [ρ_{el}]	3E-07	4E-07	$\Omega \cdot m$
Density [ρ]	7,3	7,8	g/cm ³

Through the software is possible to simulate the operative condition of the system. The first step is to constrain the system and then to apply the forces on it. The system is bounded through the iron support, exactly in the lateral and upper face of it.

The pressure acting on the pad can be represented through forces distributed on the pad. The calculus is made considering the maximum force acting on the pad during the operating conditions.

In figure 23 arrows shows the constrains (green) and forces (red) distribution applied on the system.

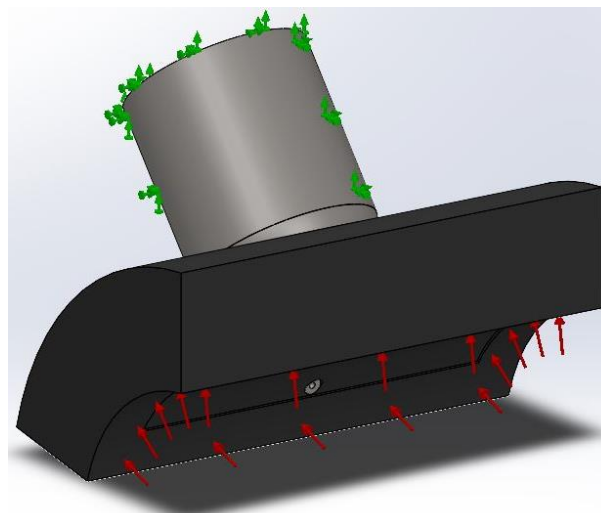


Figure 23. System constrains and pressure force distribution.

The further step is represented by the mesh, the discretization of the system by dividing it in little elements; that is the FEM characteristic. It is an automatic process, the software divides the system in many parts, in according with their size. Figure 24 represents the mesh process.

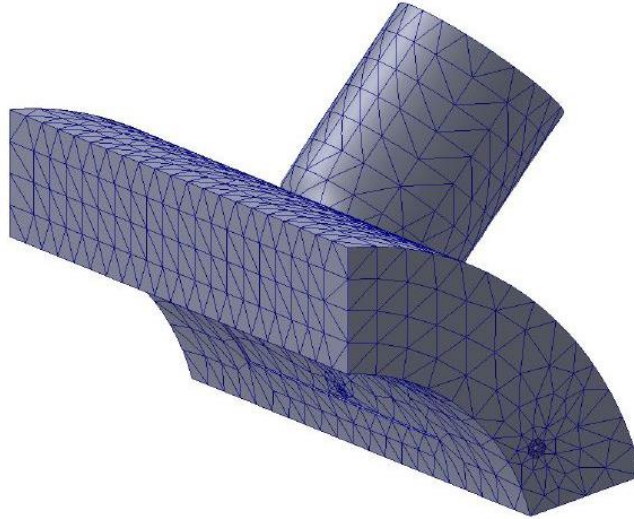


Figure 24. Mesh of the hydrostatic bearing pad.

The system is now arranged to be analyzed. At this point, the deflection analysis can be easily run and it is possible to discuss the results.

The results obtained for the two different bearing pads, subjected to a maximum pressure of 50 bar, are showed in figure 25 and figure 26. The deflection simulation of the object is represented in the center of the figure and the legend with a color distribution represents the displacement of the pad, on the right side.

The smaller pad is analyzed in the first figure and the bigger one in the second figure. It is possible to observe that the colors distribution is the same in both figures, that is mean that the pads has the same behavior to deflect. The numerical difference is given by the difference in the geometry. Basically, the bigger pad has a bigger deflection because the pad length is higher, so the effect of the pressure is more critical in a longer pad.

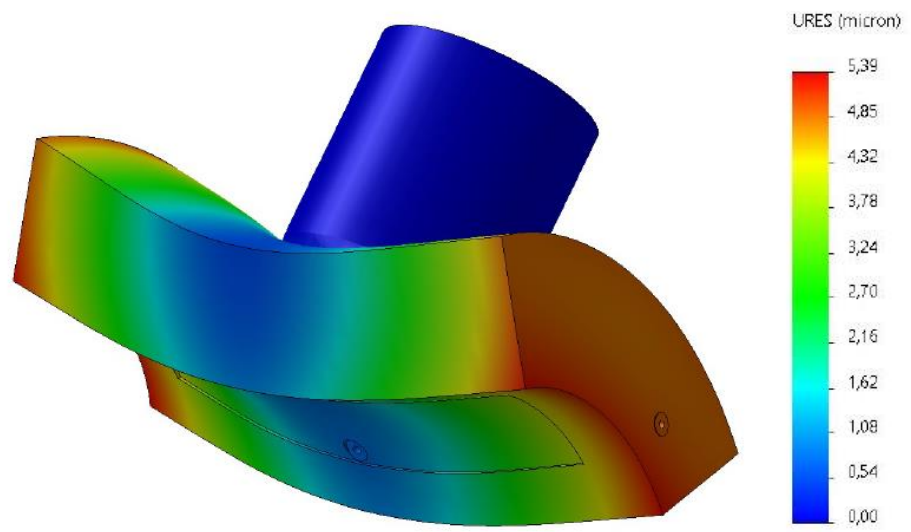


Figure 25. Smaller bearing pad deflection analysis.

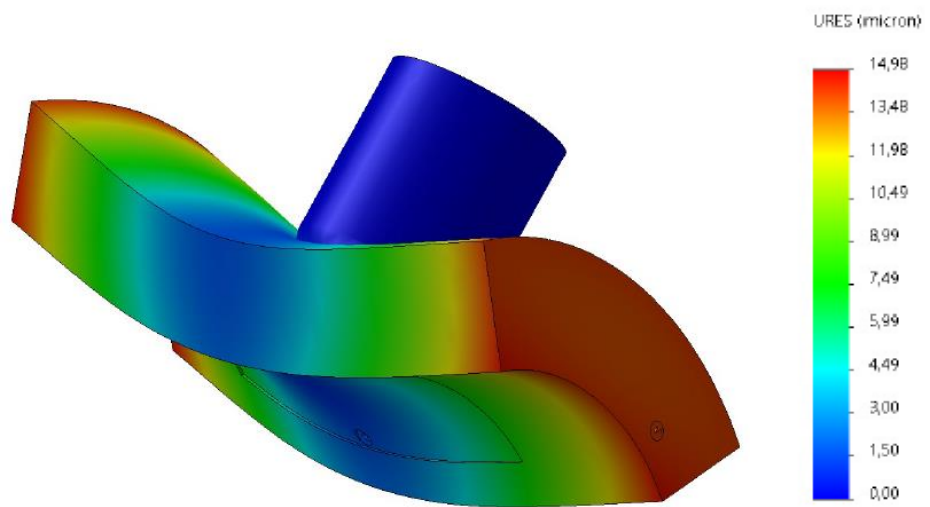


Figure 26. Bigger bearing pad deflection analysis.

3. Stiffness measurement setup

The experimental analysis purpose is to compare the theoretical data already discussed, to the experimental ones, through the method following illustrated.

The purpose of the experiment is to test the stiffness of the hydrostatic journal bearing. The easiest way to do this is to apply a force to the spindle and register the system behavior.

The idea is to generate an external force and apply it to the spindle, then to register the shaft displacement. The force is generated thanks to an electromagnetic device directly operating to the shaft, and the displacement is registered through a mechanical measuring system.

3.1 Experimental setup

The laboratory setup is really simple and it is characterized by a mechanic, an electronic and an electromagnetic equipment.

As told before, the main element to analyze is the shaft. The purpose is to apply a force to it and then register its displacement. The external force applied to the spindle is generated by an electromagnetic system, called magnet loader. The current needed by the magnet loader is given by a current actuator that receives energy from a power supply connected to the network.

Being that sensors, strain gage, acquiring data system and all other measuring elements very expensive for this application, the displacement measurement and the evaluation of the applied forces are not obtained through this equipment. Their values are registered through mechanical systems that will be shown in this chapter.

Figure 27 shows the block diagram related to the experimental setup.

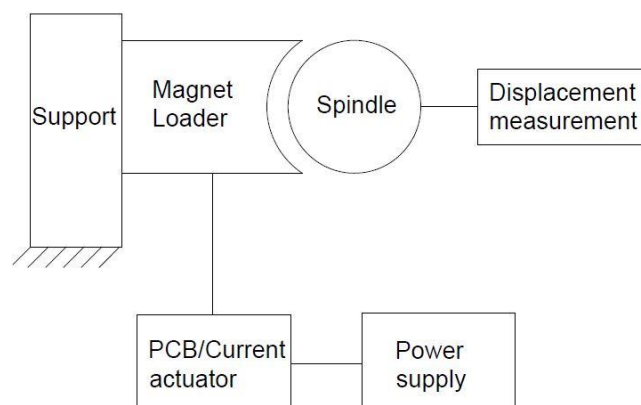


Figure 27. Block diagram of the experimental setup.

3.1.1 Magnet Loader

The non-contact type loading device (magnet loader) generates magnetic field on the inner wall of the spindle, applying an attraction force on it. The loading device is composed of iron core, coils, and housing. The iron core is a C40 iron structure, and the coils are wound around it. The structure is fixed to the frame through screws.

Electromagnetic load is a method of using magnetic field controlled by current to excite ferromagnetic substance. The basic application is electromagnet shown as figure 28. Because of the resemblance to active magnetic bearing in structure and principle, the electromagnetic force of the device can be derived by the Maxwell equation in electromagnetic field theory. When the non-saturated magnetic field is distributed uniformly throughout the air gap between electromagnet and tool and the influence of magnetic flux leakage is ignored, the magnitude of magnetic force can be simplified as the following expression [11]:

$$F = \frac{B^2 S}{2\mu_0}. \quad (25)$$

The magnetic induction intensity B in (26) is given by

$$B = \frac{\mu_0 N i}{2e}, \quad (26)$$

where S is the area of magnetic pole, μ_0 is the permeability of vacuum, equal to $4\pi \times 10^{-7} H/m$, e is the thickness of air gap, N is the coil turn, and i is the magnitude of current.

The U-shaped magnet core is applied in the device, so the resultant magnetic force is [8]

$$F = \frac{B^2 S}{\mu_0} = \mu_0 N^2 S \frac{i^2}{e^2}. \quad (27)$$

After the choice of the constant parameters N , S and e , it is possible to define the correspondence between the current i and the attraction force F , through equation (27). The constant parameters are showed in table 16.

Table 17.Parameter of the electromagnet.

Parameters		Value
Coil turns	N	450
Magnetic pole	S	3125 mm ²
Air gap	e	0,4 mm

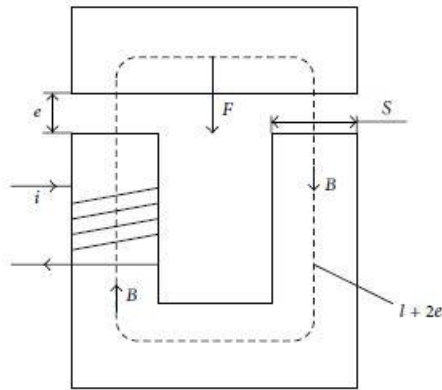


Figure 28. U-shape magnet loader.

The relation between magnetic force F , magnetic induction intensity B and current i , obtained through equations (26) and (27), is showed in table 18.

Table 18. Theoretical Force-Current relation.

i [A]	F [N]	B [T]
0,1	7	0,1
0,2	27	0,3
0,3	61	0,4
0,4	109	0,6
0,5	171	0,7
0,6	246	0,9
0,7	335	1,0
0,8	437	1,2
0,9	553	1,3
1,0	683	1,5
1,1	827	1,6
1,2	984	1,8
1,3	1154	1,9
1,4	1339	2,1
1,5	1537	2,2
1,6	1749	2,4
1,7	1974	2,5
1,8	2213	2,7
1,9	2466	2,8
2,0	2733	3,0
2,1	3013	3,1

2,2	3306	3,2
2,3	3614	3,4
2,4	3935	3,5
2,5	4270	3,7
2,6	4618	3,8
2,7	4980	4,0
2,8	5356	4,1
2,9	5745	4,3
3,0	6148	4,4
3,1	6565	4,6
3,2	6995	4,7
3,3	7439	4,9
3,4	7897	5,0
3,5	8368	5,2
3,6	8853	5,3
3,7	9352	5,5
3,8	9864	5,6
3,9	10390	5,8
4,0	10930	5,9
4,1	11483	6,1
4,2	12050	6,2
4,3	12631	6,3
4,4	13225	6,5
4,5	13833	6,6
4,6	14455	6,8
4,7	15090	6,9
4,8	15739	7,1
4,9	16402	7,2
5,0	17078	7,4

This theoretical force-current correspondence must be evaluated in the experimental model and a real correspondence between force and current must be done. The calibration process is very important to guarantee the right force we want to apply to the spindle.

The magnet loader was realized inside the company. After the realization of the iron core, it has been fixed to a circular element and then rotated to allow the cable to be wound up, as shown in figure 29.



Figure 29. Magnet loader (electromagnet) with 450 coils.

3.1.2 External force evaluation

Considering that the magnet loader generates an attraction force, the whole electromagnetic system is attracted to the metallic spindle. Fixing the magnetic system to a flexible support, and knowing the rigidity of the support, is possible to find the attraction force the magnet generate, in function of the given current. Obviously, at a zero-current condition, the distance between spindle and electromagnet must be bigger than the support maximum deflection, to avoid contact between the surfaces.

Connecting the magnet loader to a metal plate and fixing the plate to a rigid support (figure 30), it is possible to evaluate the plate arrow for any kind of generated force. For each value of current given to the electromagnet, a measurement of the deflection of the metal plate was made. Then multiplying the arrow for the plate stiffness, it is possible to know the correspondence between current and attraction force.

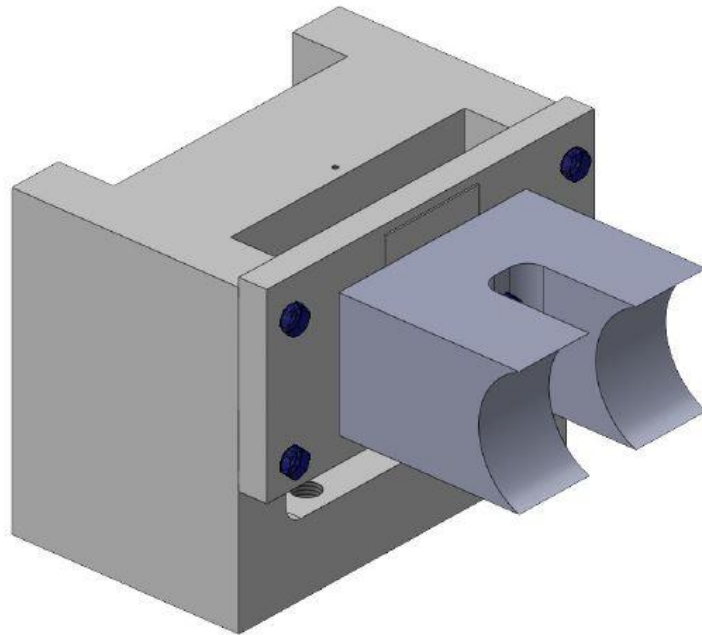


Figure 30. External load generator.

To evaluate the deflection of the metal plate, a traditional measuring system is involved. Though a digital feeler gauge with millesimal resolution is possible to measure the distance between the fixed structure and the deformed plate.

Installing keys on both structures – one fixed and one moving, it is possible to measure the relative distance between them, under different load conditions.

Looking at figure 31, the keys are represented by the green elements. The left one is fixed and the right one changes its position according to the metal plate deflection.

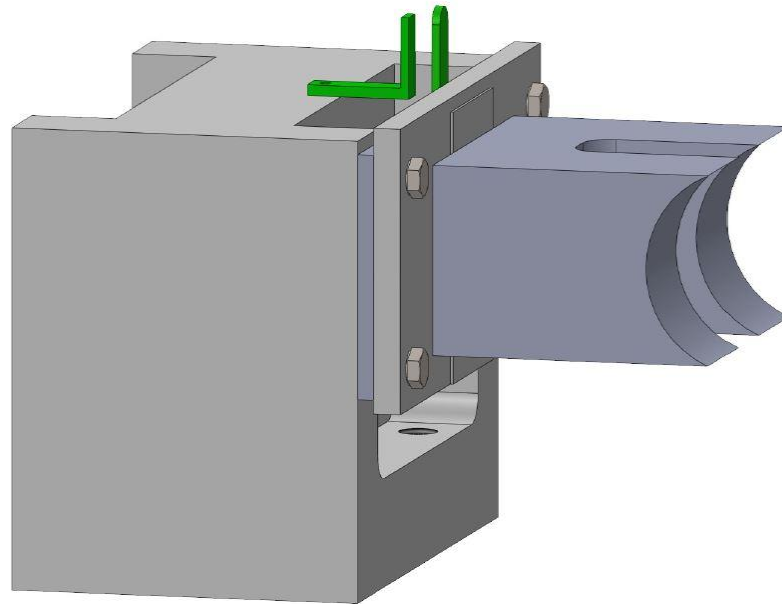


Figure 31. Generator and measuring system of external loads.

Considering a 210x105x10 mm metal plate laterally supported by two 90x30 mm platelets and fixed by four screws, the plate rigidity can be detected by considering both arrows due to fixed beam and supported beam cases and then averaging those results to obtain the mean of the arrow, so the plate stiffness.

The stiffness of the plate is approximately 70 N/ μm and its deflection due to the current load is shown in table 19. The measuring instrument for plate displacement is showed in figure 32.

Table 19.Relation between current on coils and plate arrow. The force is deducted through the plate stiffness.

Current (A)	Plate arrow (μm)	Electromagnetic force (N)
0,8	1,5	102
0,9	4,2	289
1	7,5	510
1,1	9	612
1,2	12,5	850
1,3	14,7	1003
1,4	17	1156
1,5	21	1428

1,6	25,2	1717
1,7	29,5	2006
1,8	33	2244
1,9	36,5	2482
2	39,7	2703
2,1	43	2924
2,2	44	2992
2,3	50	3400
2,4	51	3468
2,5	55	3740
2,6	58	3944
2,7	60,2	4097
2,8	62,5	4250
2,9	64	4352
3	66,5	4522
3,1	68,7	4675
3,2	71	4828
3,3	73	4964
3,4	75	5100
3,5	77	5236
3,6	77	5236
3,7	81	5508
3,8	84	5712
3,9	85	5780
4	86,5	5882



Figure 32. Digital feeler gauger with millesimal resolution used to calculate the plate arrow.

The digital feeler gauger datasheet is reported on Appendix B.

3.1.3 V-I (Voltage to Current) Converter

As told before, the electromagnetic device works thanks current that flows inside the coils. To allow the generation of the magnetic force on the spindle, the wrapped coils need to be supplied by current.

To control the process and to guarantee to give the right current value to the system, a V-I (Voltage to Current) converter was realized. The aim of this circuit is to convert and regulate an input voltage to an output current that can be used to control the electromagnetic device. Basically, through an adjustable voltage generator, it is possible to adjust the output current.

Thanks to the project files and bill materials offered by *Texas Instrument*, the circuit components were bought and then assembled by the tin soldering. The electrical schematic is showed in figure 33 in a simple version. The realized PCB (Printed Circuit Board) is showed in figure 34 and its technical specification are reported in table 20.

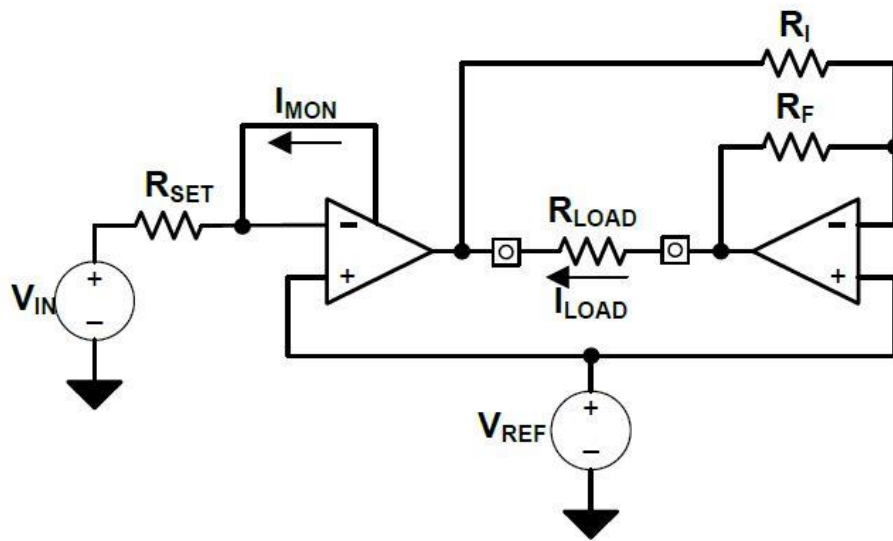


Figure 33. Simplified V-I converter circuit schematic.

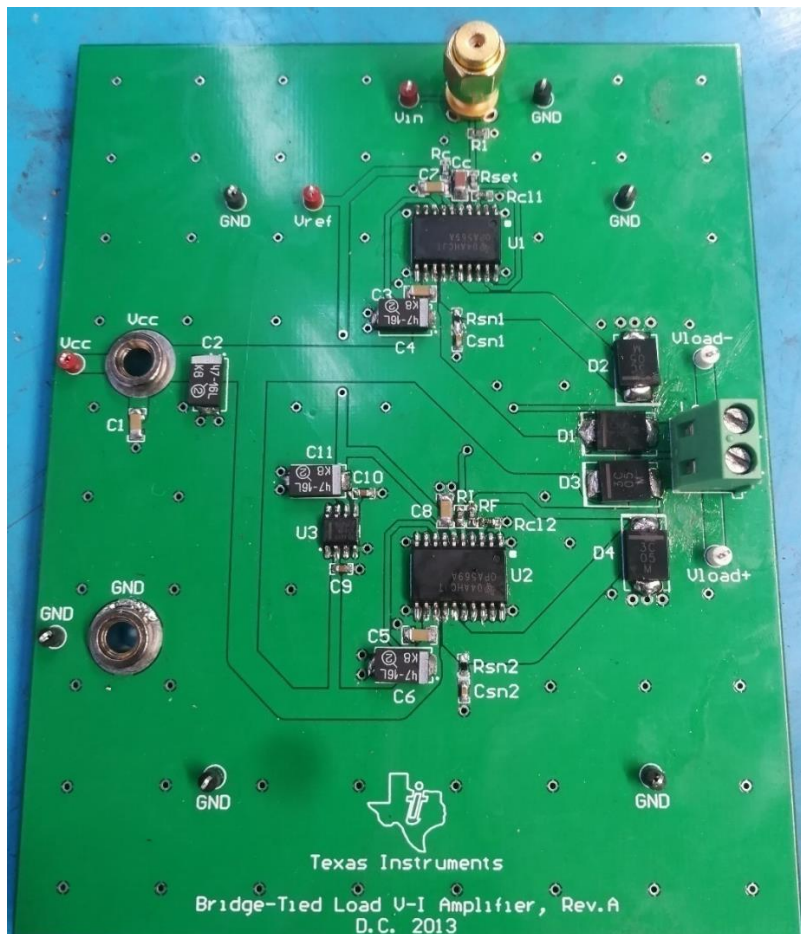


Figure 34. Homemade Texas Instrument V-I amplifier PCB.

Table 20. V-I Converter technical specification.

	Symbol	Value
Voltage supply	V_{IN}	5 V dc
Input voltage	V_{REF}	0 – 4,5 V dc, zero-scale output at 2,5 V dc
Output current	I_{LOAD}	+/-2 A dc

Before connecting the magnet loader to the V-I converter, a test of the device was conducted. Different resistors were connected to the output of the PCB to simulate the real condition, according to the magnet loader resistance.

The terminals of the wrapped coil around the magnet loader are connected to the PCB terminal blocks. The I_{LOAD} represent the current value to give to the electromagnetic system, and it is controlled by an adjustable power supply through a potentiometer.

The adjustable DC power supply that allows to regulate the input signal is showed in figure 35.



Figure 35. Adjustable power supply used in laboratory.

3.1.4 Displacement measurement

The spindle displacement measurement is made through a micrometric dial indicator. It works through a sliding shaft and the translation of the shaft correspond to a change in position of the object under measurement. Calibrating it and placing it in the same direction of the external load, and in contact with the spindle, the dial indicator indicates the amount of the spindle displacement, when load occurs.

Due to the limited dial indicator resolution, comparing it to the displacement of the spindle (tens of microns) the tool is not the best solution for this application, but the finest we had.

Figure 36 shows the measurement device.



Figure 36. *Micrometric dial indicator device.*

4. Arrangement and experimental results

4.1 Preparation

Thanks to the machinery available within the company, every single component was made in-house. Turning and milling were the main operations to allow the realization of the pieces.

In order to prevent oxidation of all metal elements, the process of burnishing of materials was carried out. After that, the preparation and the assembly of the system were performed.

4.1.1 Elements of the system

The main elements to the mechanical system are the hydraulic power unit, a stopper that operate as a distribution channel for the oil (it basically receives the oil in pressure from the hydraulic power unit and send it to the three pads), the pipes that link the stopper to the bushings, the bushings (figure 37 and 38), the struts (figure 39) to regulate the clearance between spindle and bushings, the spindle, and the cases (figure 40).

When the shaft is in rotation, it is important to prevent the contact between it and the pads, to avoid seizure. To allow this, it is important to smooth the surface of potentially contacting parts, to reduce the damage. Plus, the smoothing operation allows to have a better oil seal between the shaft and the pads.

Being that the machines used to realize the components has a decimal precision, the grinding operation, that has a millesimal precision and make the surface smooth, must be done.

For the shaft, the process was easier than the pads because of the geometry and the treatment has been committed. As regards the bushings, the operation was made internally by hand, through the scraping of the pads.

The operation involves putting a colored product - called engineering blue, on the shaft and then press the bushing onto it to see the contact in detail. If the contact between the pieces is poor (little blue), the scraping of the pad must be done. The process is repeated until the color is uniform on the bushing. The process is showed through pictures in appendix C.

Because of the impossibility to assembly the system piece by piece at the same time, due to the small space inside the case, a subsystem is assembled first.

To avoid leakage between the various connections, O-rings are provided. The gaskets are held against the wall by screws on which a through-hole is drilled to pass the pipe (figure 41).

Initially, the pipes are pre-assembled with the stopper and then the stoppers are inserted in the case (figure 42 and figure 43).

After mounting O-ring into the pads, bushings are connected to the pipes, inside the case. Then struts can be screwed on (figure 44) and they can finally support the pads (figure 45).

The whole assembled system is showed in figures 46 and 47. Figure 48 shows the experimental setup after machine assembling, including the measuring system.



Figure 37. Small bearing pads.



Figure 38. Big bearing pads.

The realized bushings present some imperfections due to the machining methodology. The support hole and the cut of the pad were made in different axes, giving less precision to the pieces. In this

way the pad does not present symmetry: the bearing lands have not the same dimension and the hole is not centered in the piece. This brings the system to inefficiencies, especially at high pressures.



Figure 39. Regulation struts.

A problem related to the struts is due to the pitch. The pitch is function of the clearance between the spindle and the pads. The oil film thickness is regulated through the pitch of the struts. Being that the clearance is of the order of microns, the pitch should be as smaller as possible to increase the accuracy on regulation.



Figure 40. Cases and metal plate before burnishing operation.



Figure 41. Drilled screws to allow O-ring crushing.



Figure 42. Pipes and stopper preassembly.

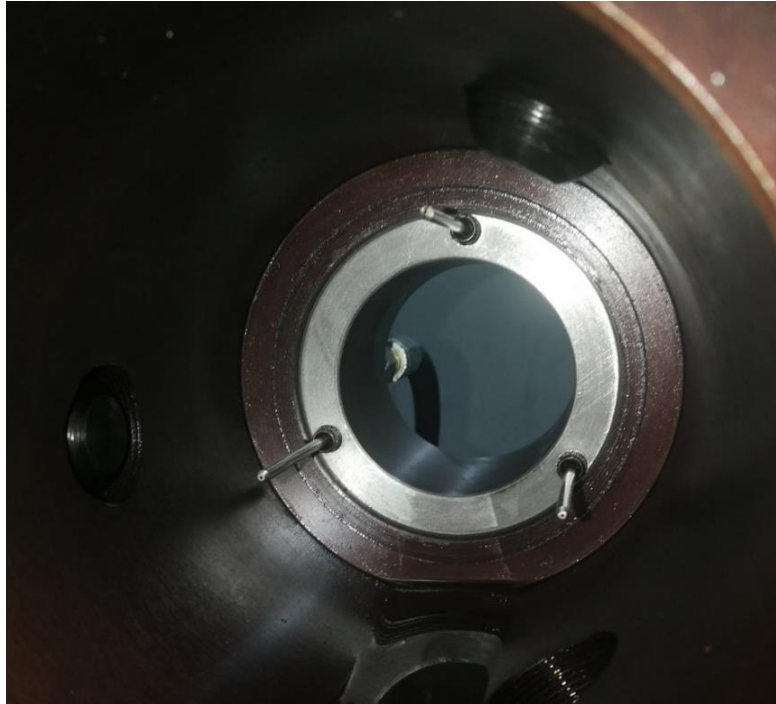


Figure 43. *Assembly of the stopper into the case.*

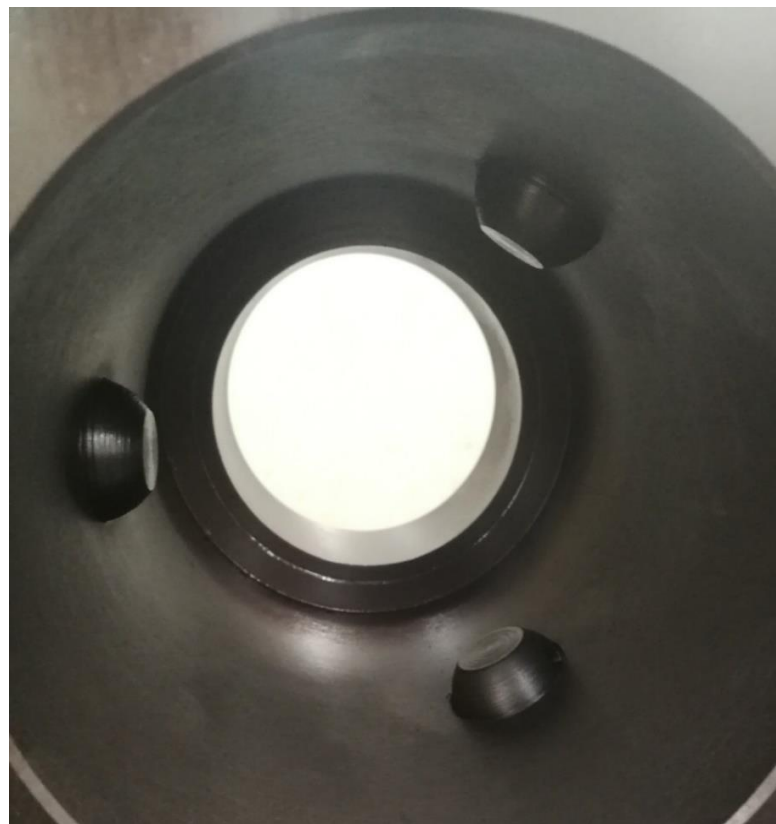


Figure 44. *Struts mounted inside the case.*



Figure 45. Bushings assembled inside the case.

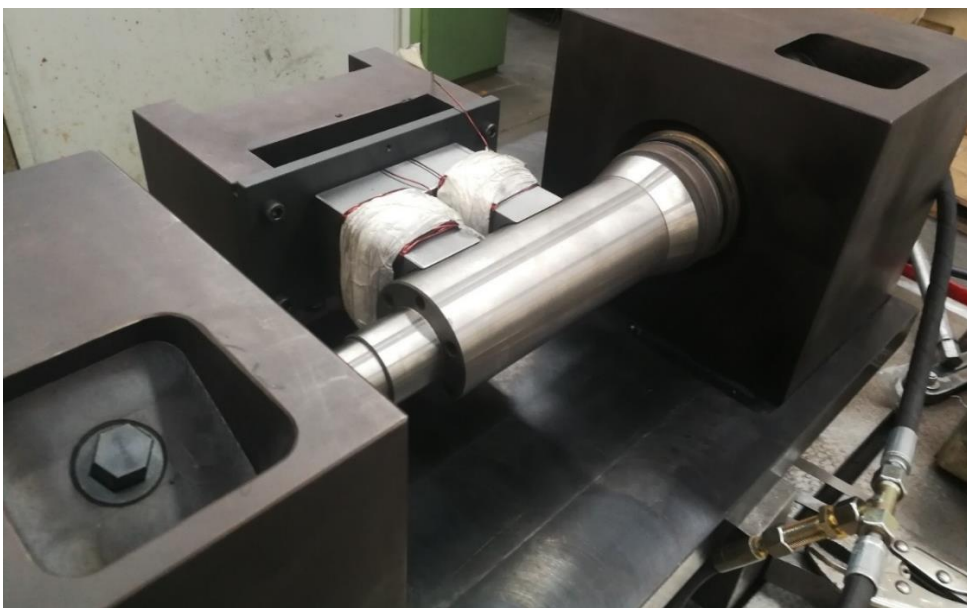


Figure 46. Assembled hydrostatic journal bearing.

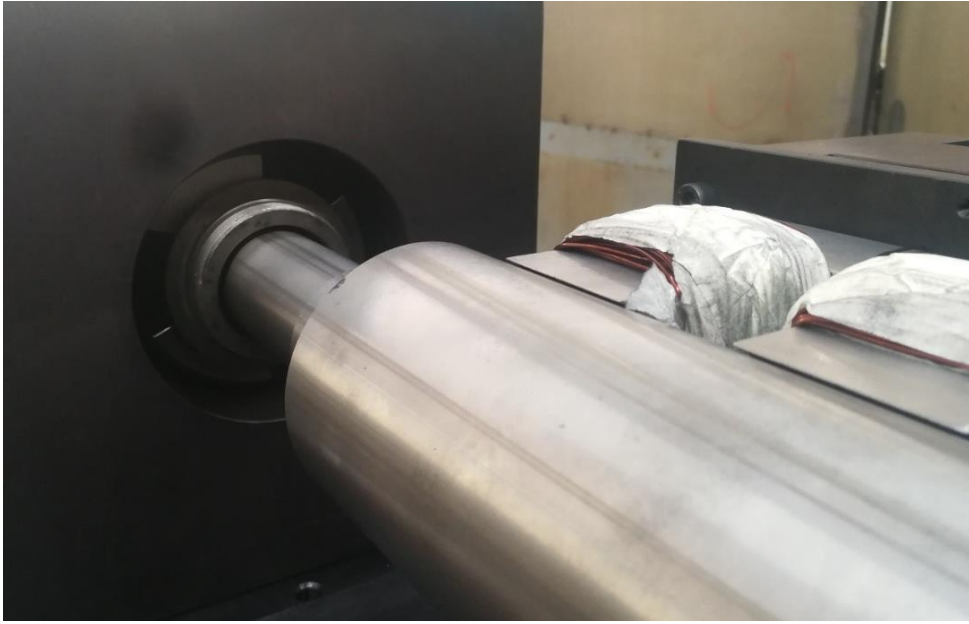


Figure 47. Detail of the assembled machinery.

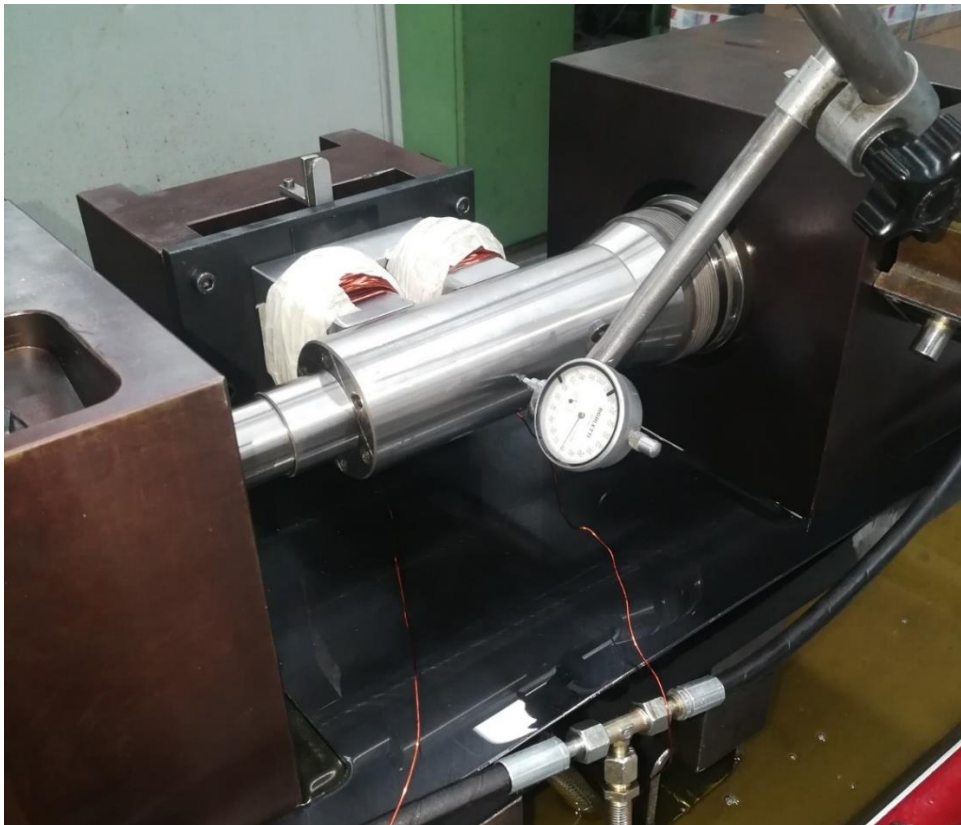


Figure 48. Experimental setup, including the measuring system.

4.1.2 Getting ready

The experimental test consists of generating different external loads to the hydrostatic spindle and then register the spindle displacement.

The load is regulated through the current signal variation. According to the theoretical force the magnet loader can generate, different values of current were applied.

Due to reproduce the theoretical load and stiffness characteristic of the system, the given values of current are chosen according to the project.

The correlation between current and electromagnetic force was the starting point of the analysis. The current was varied by steps of 100 mA and the force correspondence to the current was registered.

To ensure the design air gap between the magnet loader and the spindle, flexible spacers were used. Several decimal spacers were used to control the space between the elements and when the air gap was too big, another spacer was inserted, this time between the metal plate and the magnet to reduce the air gap and bring it to the desired air thickness.

The difference between the experimental and the theoretical curve could be due to the imperfect concentricity between the magnet loader and the spindle, figure 49.

Considering a pressure supply $P_s = 50$ bar and the design film thickness $h_d = 30 \mu\text{m}$, force and stiffness characteristics for both pad types are showed in figure 50 and figure 51. A comparison between different clearance of the system is showed in figure 52 and figure 53, where the design characteristics of the whole system are showed, for a design oil film thickness of $30 \mu\text{m}$ and $15 \mu\text{m}$.

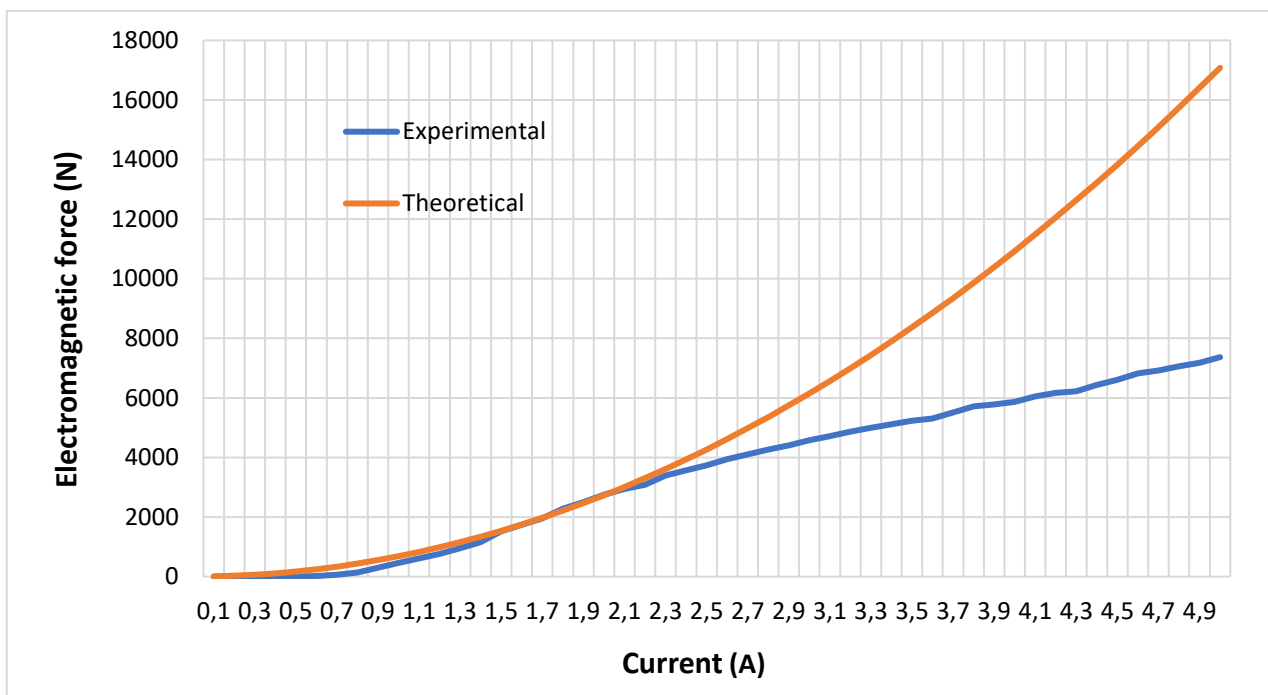


Figure 49. Relation between current in the coils and electromagnetic force generated by the magnet loader.

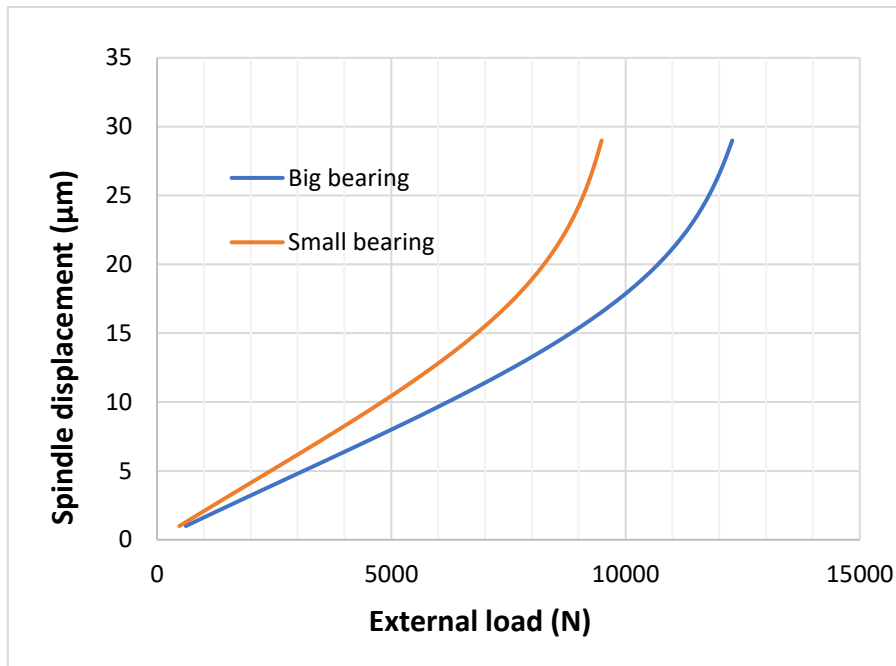


Figure 50. Spindle displacement characteristics for each bearing. $P_s = 50$ bar, $h_d = 30$ μm.

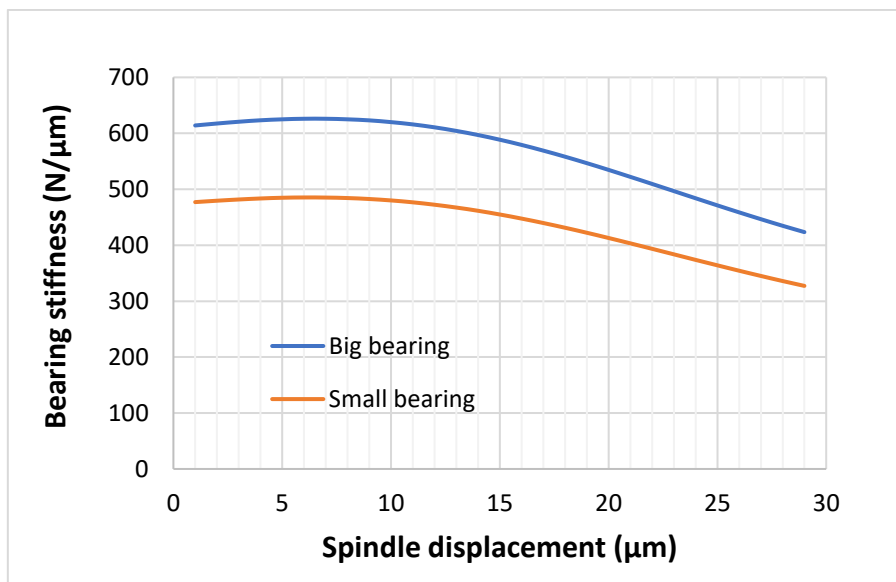


Figure 51. Stiffness characteristics for each bearing. $P_s = 50$ bar, $h_d = 30$ μm.

The difference between the two curves depends on the different geometry of each pad. At the same pressure, the big pad has a larger equivalent area and therefore it generates greater resistance to external loads, so higher stiffness.

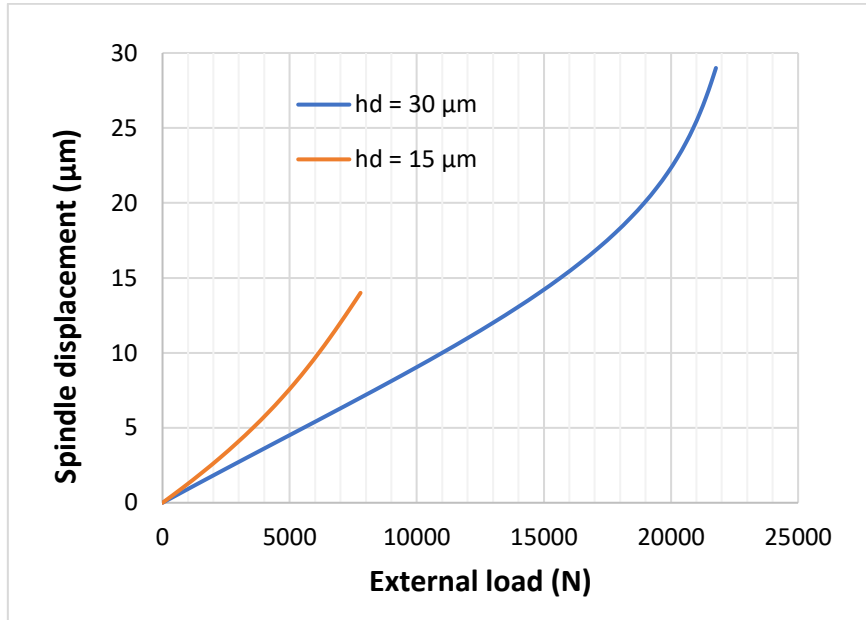


Figure 52. Spindle displacement characteristics of the system. $P_s = 50$ bar.

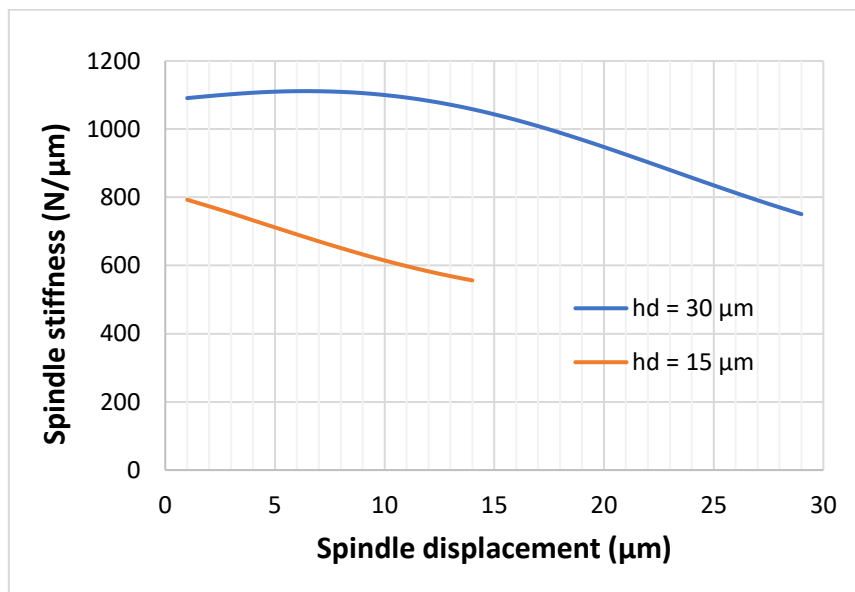


Figure 53. Stiffness characteristics of the system. $P_s = 50$ bar.

Leaving the other parameters of the system unchanged, when a change of the design oil film thickness occurs by reducing it to a smaller one, the behavior of the system gets worse. In reality,

for this project the oil film thickness of 30 μm represent the best solution for the system, so also increasing instead of decreasing the clearance, the stiffness decreases.

The designed system allows to modify the oil film thickness through the struts. Due to the concentricity of the bearings, it is possible to adjust only one strut and obtain the desired film thickness. Through a proportion, is possible to calculate the angle rotation of the strut to choose the gap. Starting from a zero-clearance condition and then correctly rotating the strut, the desired oil film thickness is reached.

Another aspect to be considered is due to the bending of the shaft. This phenomenon greatly influences the measurements. To avoid inconsistencies in the behavior of the system, it is necessary to perform a measurement of the deflection. The process consists of giving the system a film gap of 0 micron, so that the flexion is not affected by the effects of pressure.

This way, a difference between the experimental data and the effect of the shaft deflection will lead the real spindle displacement. Figure 54 shows an example of the conducted measurement to tackle the problem.

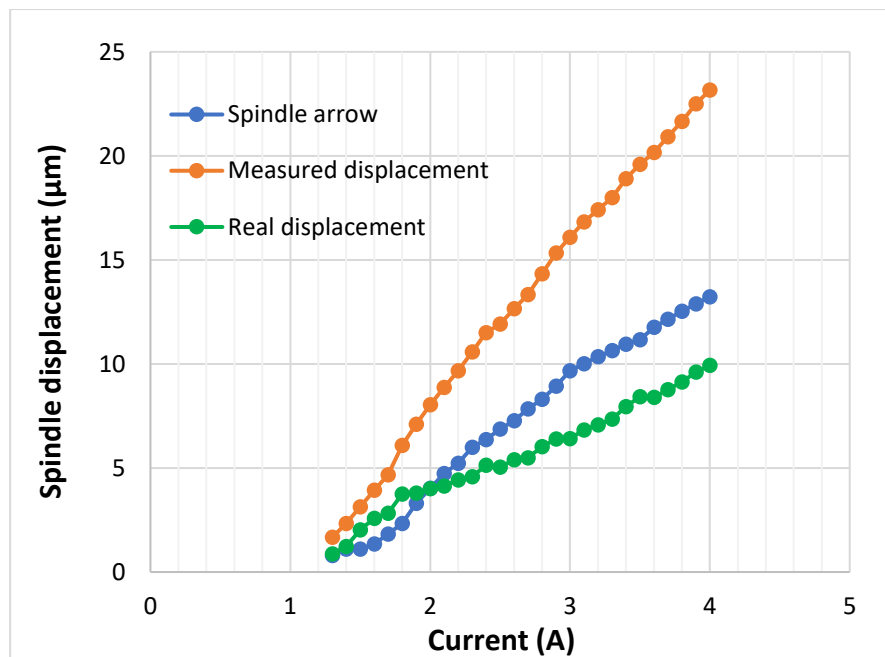


Figure 54. Spindle arrow compensation.

4.2 Results

After connecting every piece in the right place, including the connection between magnet loader with the current amplifier, and the calibration of the system, the test started.

It consists of the generation of different stresses to the spindle through varying the current in the power amplifier.

The machinery has been designed to operate at a supply pressure of 50 bar and the main test are carried out based on this value. To validate the theoretical study, tests were also conducted at a lower supply pressure.

On appendix B a summary table is presented. Table 23 and table 24 show the experimental data related to $h_d = 30 \mu\text{m}$ and $h_d = 15 \mu\text{m}$, respectively and it includes the relation between current, electromagnetic force, spindle displacement and stiffness.

Due to the limited tools, the oil film thickness regulation was not really accurate, so it is possible that the experimental results that will be discussed are not exact, and they softly differ to the reality.

By the way, the behavior of the real system is described in the following subchapters where a comparison with the theoretical model appears.

Tests were done considering the design characteristics of the system, but some features were changed to evaluate the theoretical model.

In this analysis, it must be considered that the design condition refers to a supply pressure of 50 bar and an oil film thickness of 30 microns. Any conditions that differ from these data are to be considered an off-design and therefore are not optimized to perform at their best. Tests at different conditions are performed to validate the design process.

Due to the magnet loader limitation, it was not possible to reproduce the whole behavior of the system, especially for 30-microns film gap, because the magnetic force required to completely displace the spindle is greater than that generated by the electromagnet.

Main tests are made varying pressure supply from 30 bar till 50 bar and changing the design film thickness.

Each measurement was conducted three times.

4.2.1 Design film thickness 30 microns

In this section the experimental data referring to a 30-microns design film thickness will be discussed. Tests are conducted at 30, 40 and 50 bar and the experimental data are compared to the theoretical ones.

For each pressure, the behavior of the spindle is showed. It includes the load characteristic, referring to the amount of the spindle displacement in relation to the external load, and the stiffness characteristic, referring to the spindle stiffness in relation to the spindle displacement.

First test is performed at supply pressure of 30 bar. Figure 55 shows the load characteristic and figure 56 shows the stiffness characteristic.

The registered spindle reaction to external load follows very good the theoretical behavior, and the real system seems to react better than the project when an external load between 2 and 5 kN acts on it.

As regard stiffness, the obtained results are not much accurate to describe the theoretical curve because of the high accuracy in measurement needed, but the average of the experimental curve basically represents the analytic data.

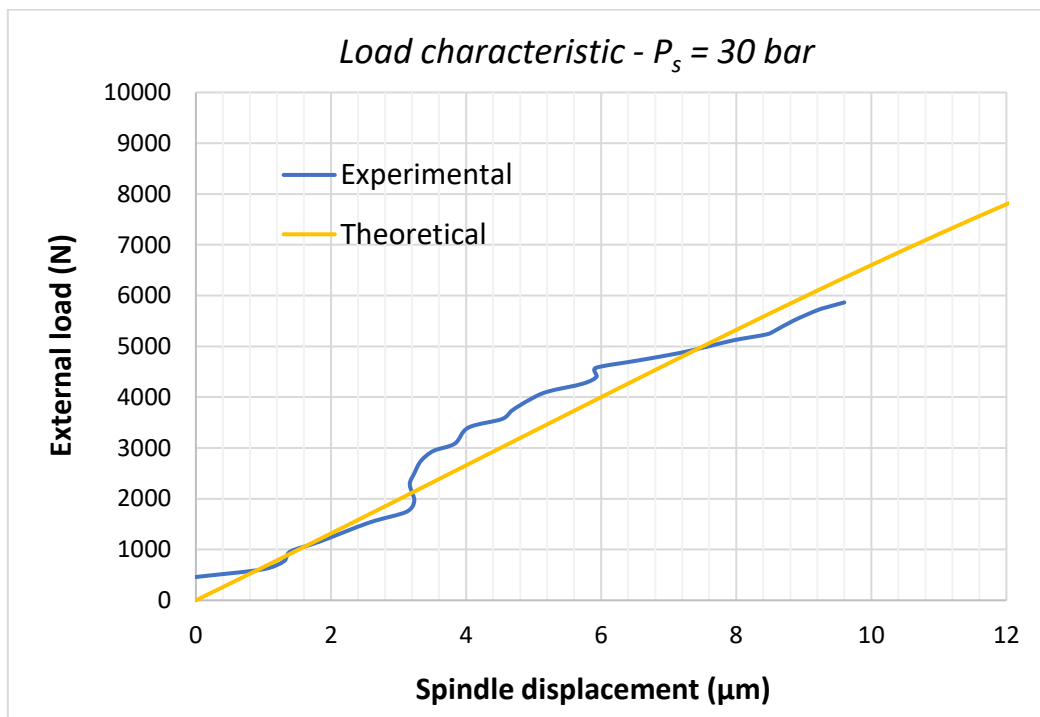


Figure 55. Hydrostatic spindle force-displacement relation between experimental and theoretical behavior. $P_s = 30$ bar, $h_d = 30$ μm.

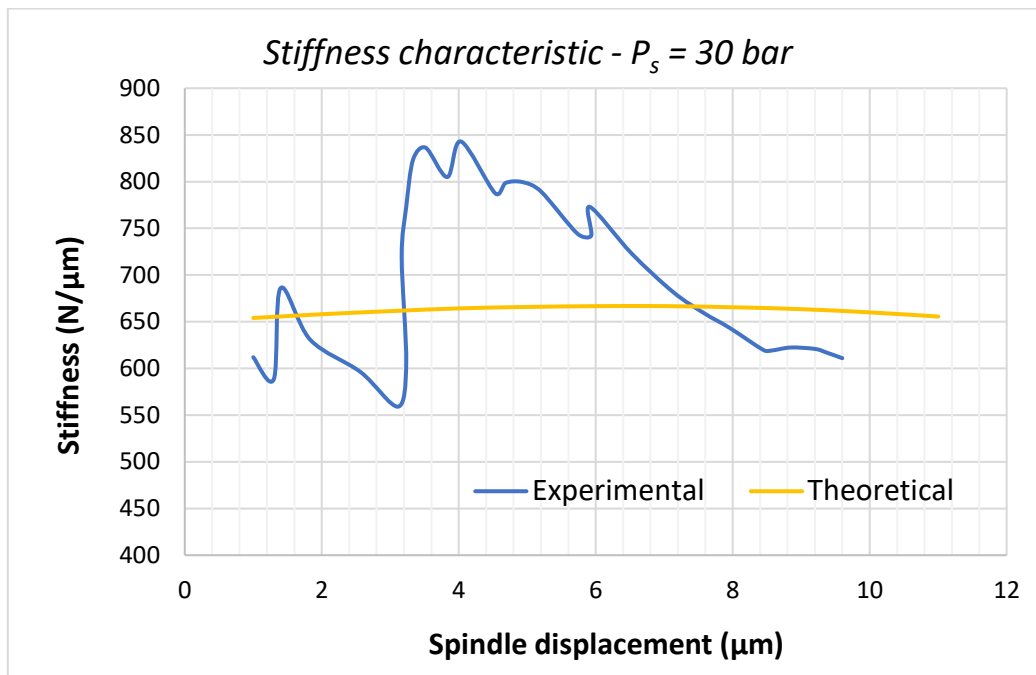


Figure 56. Hydrostatic spindle stiffness-displacement relation between experimental and theoretical behavior. $P_s = 30$ bar, $h_d = 30$ μm.

In the second test the pressure was increased by 10 bar and the obtained data are illustrated in figure 57 and figure 58, where the load characteristic and stiffness characteristic are respectively showed.

The system works very well when the displacement of the spindle is smaller than 6 microns, after that it seems that the rigidity of the system decreases, but the magnet loader limitation does not allow to obtain a spindle displacement bigger than 8 μm to understand better the behavior.

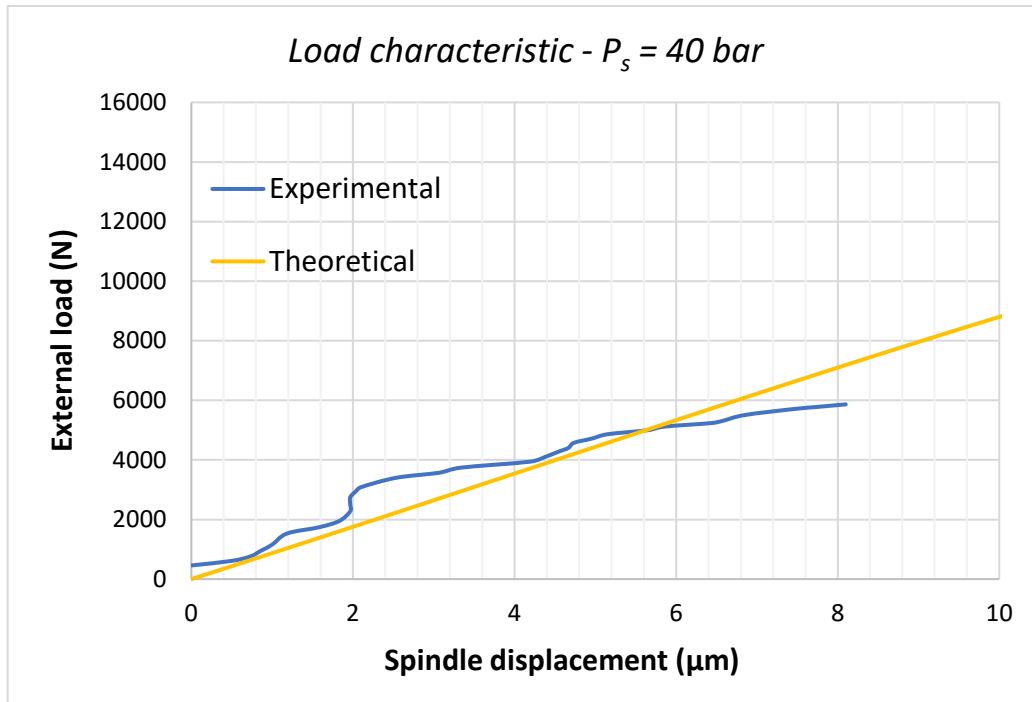


Figure 57. Hydrostatic spindle force-displacement relation between experimental and theoretical behavior. $P_s = 40$ bar, $h_d = 30$ μm.

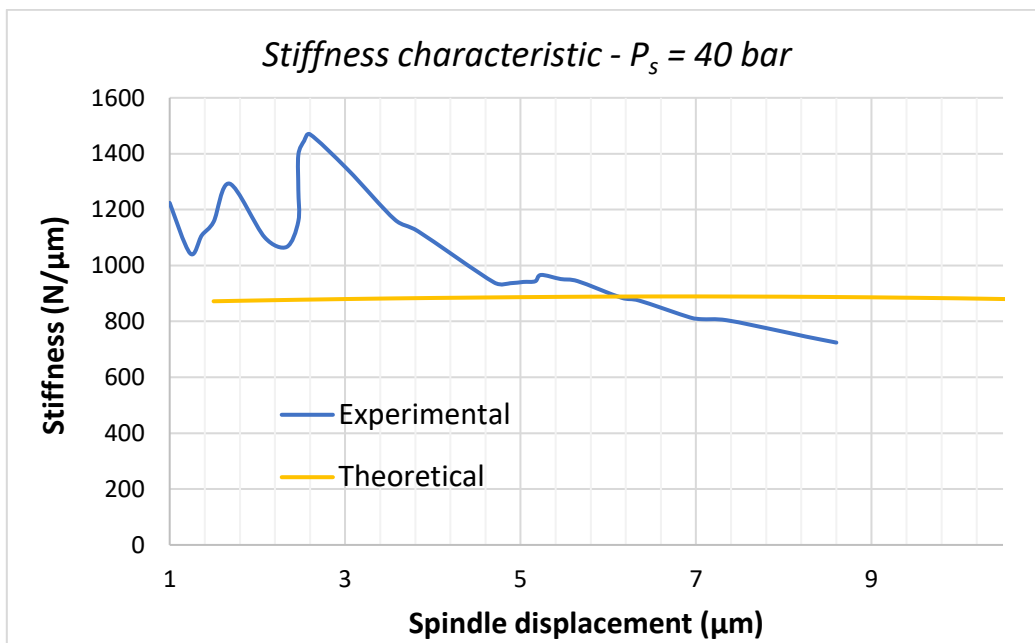


Figure 58. Hydrostatic spindle stiffness-displacement relation between experimental and theoretical behavior. $P_s = 40$ bar, $h_d = 30$ μm.

Last test for 30 microns oil gap is executed at a pressure supply pair to 50 bar and it corresponds to the design condition. Figure 59 and figure 60 represent the load and stiffness characteristic, respectively.

The experimental results do not correspond to the analytical ones, this is probably due to leakages between the connection of the system that increase with the pressure. Another factor that influences the inefficiency of the system is due to the pump limitation. The motor linked to the pump is not designed to work to a 50-bar condition, so probably back-pressure acts on the system.

Moreover, the asymmetry of the bushings and the difference between the width of the lands are the main problem of the inefficiency of the system. This imperfection on the pads causes a non-homogeneous distribution of pressure that create leakages through the pads, so the stiffness decrease.

Looking at the stiffness characteristic the difference between theoretical and experimental data clarifies the curves gap.

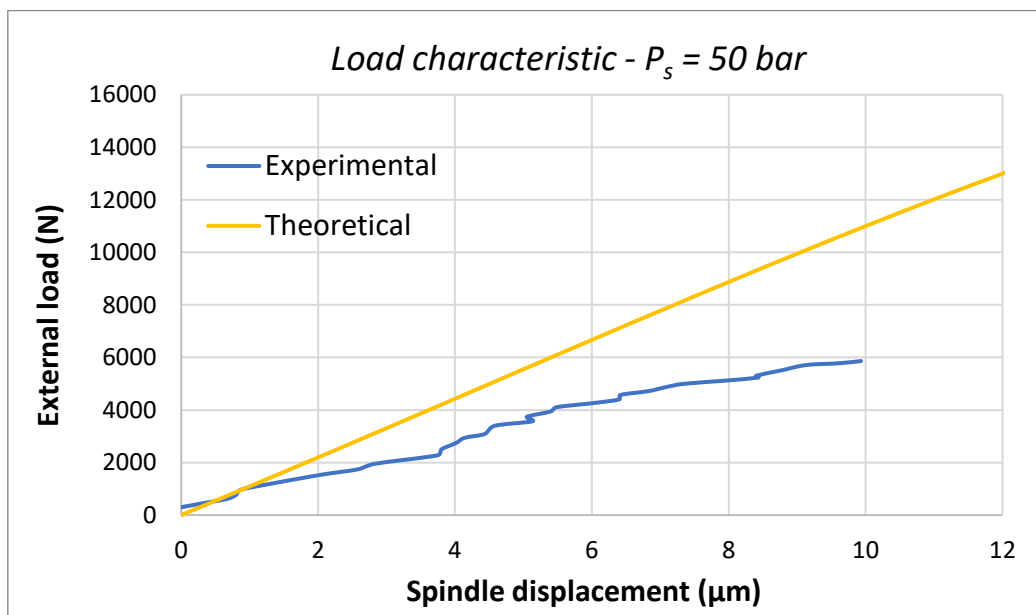


Figure 59. Hydrostatic spindle force-displacement relation between experimental and theoretical behavior. $P_s = 50$ bar, $h_d = 30$ μm.

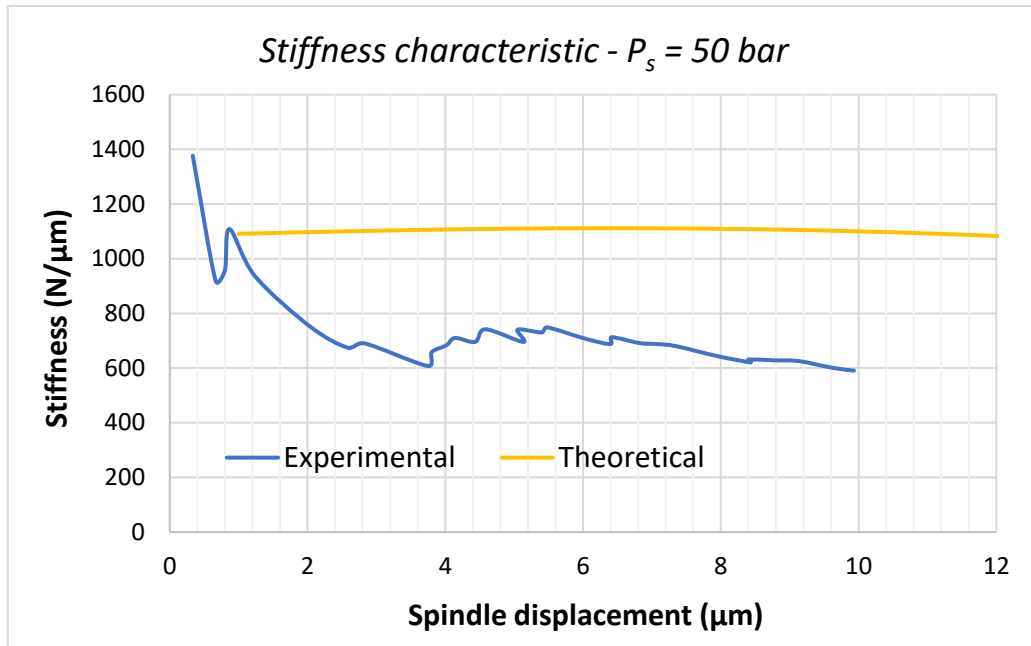


Figure 60. Hydrostatic spindle stiffness-displacement relation between experimental and theoretical behavior. $P_s = 50$ bar, $h_d = 30 \mu\text{m}$.

4.2.2 Design film thickness 15 microns

The already discussed tests were conducted changing the oil gap between the pads and the spindle.

In this section the experimental data referring to a 15 microns film thickness will be discussed. Tests are conducted at 30, 40 and 50 bar and the experimental data are compared to the theoretical ones.

It is important to underline that since the thickness of the oil film is very small (15 microns), it was not possible to adjust it accurately and the results could differ from the desired condition.

The results referred to 30 bar tests are showed in figure 61 and figure 62.

It is possible to see that the trend of the curve has a step corresponding to about 5 microns displacement. Now, considering that after 5 microns spindle displacement, the trend of the experimental curve follows the theoretical although shifted upwards, the non-linearity depends on the poor resolution of the measuring instrument.

Considering this, the experimental results represent better the behavior of the system. This could depend to an inaccurate regulation of the oil film thickness.

Even looking at the stiffness characteristic is possible to see that the experimental data have the same shape of theoretical data but shifter upwards.

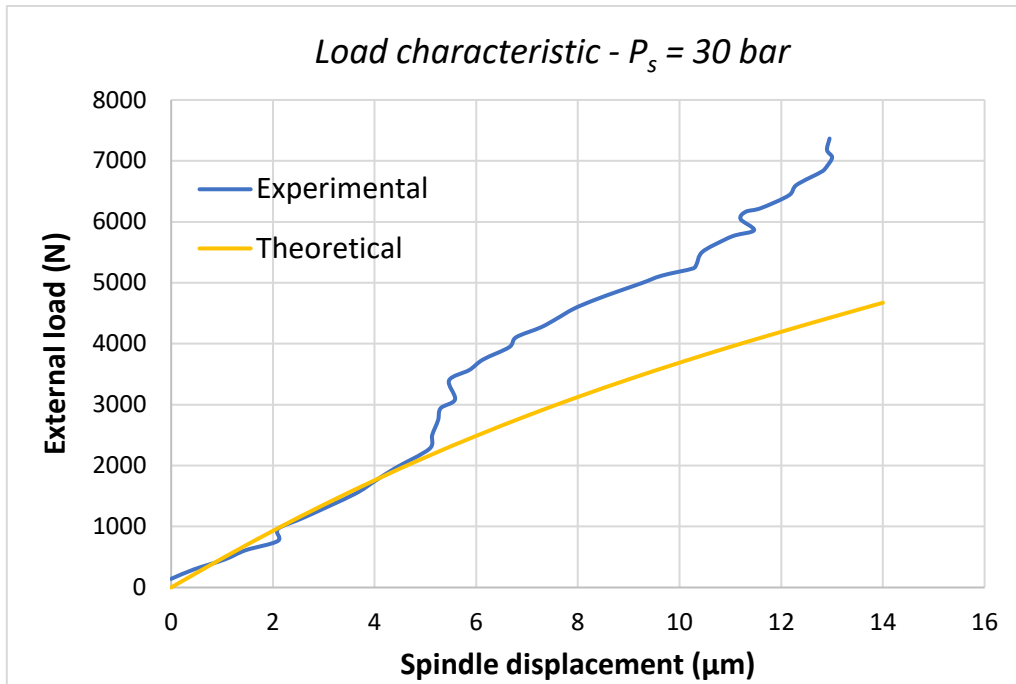


Figure 61. Hydrostatic spindle force-displacement relation between experimental and theoretical behavior. $P_s = 30$ bar, $h_d = 15\mu\text{m}$.

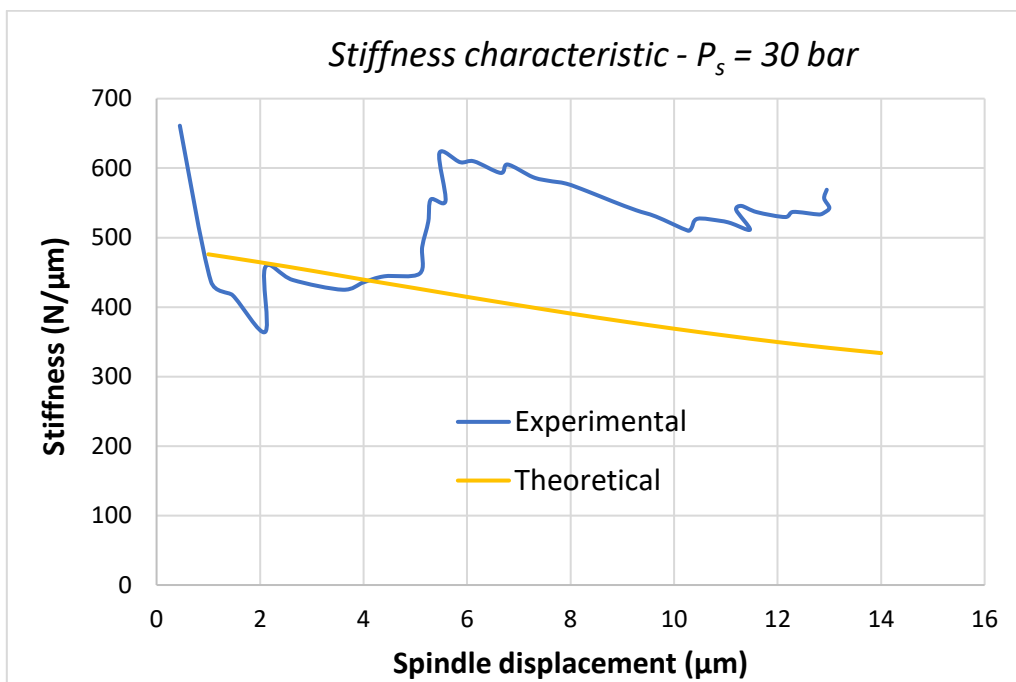


Figure 62. Hydrostatic spindle stiffness-displacement relation between experimental and theoretical behavior. $P_s = 30$ bar, $h_d = 15\mu\text{m}$.

The test conducted at 40 bar supply pressure shows a good correspondence between experimental results and design characteristic. As told before, the measurement referring to small spindle displacement is not accurate and for this the curve do not fit good at the beginning.

Looking both figure 63 and figure 64 is possible to notice that when a spindle displacement of 13 microns occurs, the experimental shape represents a better behavior than the theoretical curve, this can depends on both the imprecision of the oil film adjustment and the better precision of the measuring instrument for larger displacements.

On the other hand, looking at figure 64, it is possible to see how for small displacement, the measurement is understimted, due to the resolution of the instrument.

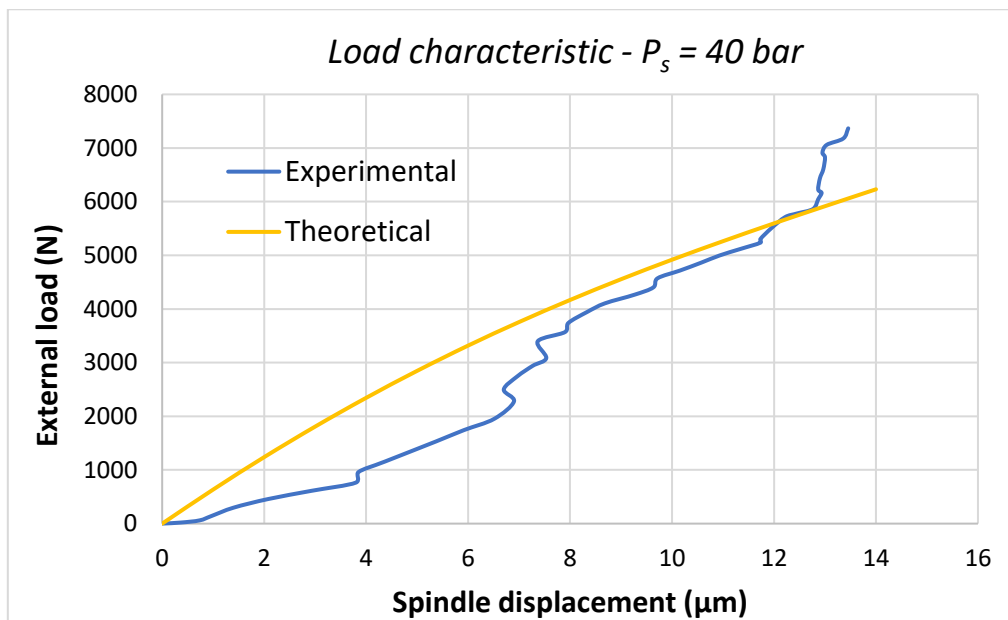


Figure 63. Hydrostatic spindle force-displacement relation between experimental and theoretical behavior.
 $P_s = 40 \text{ bar}$, $h_d = 15 \mu\text{m}$.

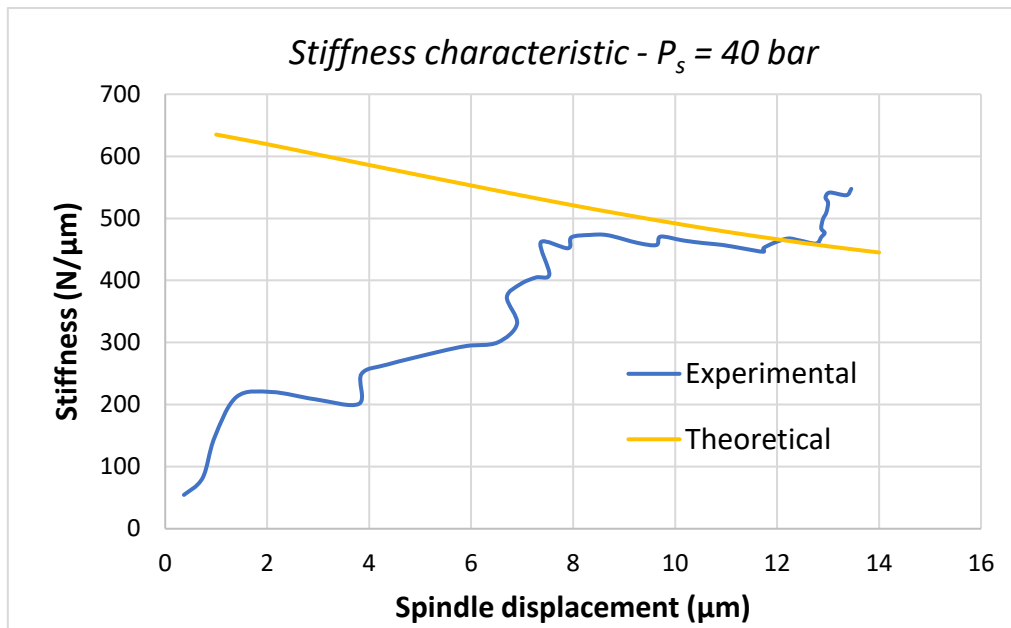


Figure 64. Hydrostatic spindle stiffness-displacement relation between experimental and theoretical behavior. $P_s = 40$ bar, $h_d = 15\mu\text{m}$.

By observing now the results referring to a pressure supply of 50 bar - figure 65 and figure 66 – is possible to notice that the load characteristic of the system perfectly fits the theoretical behavior. The same cannot be said for the stiffness characteristic, where in the left side of the graph the experimental results show discrepancy to the theoretical ones, as a result of the poor resolution of the measuring instrument.

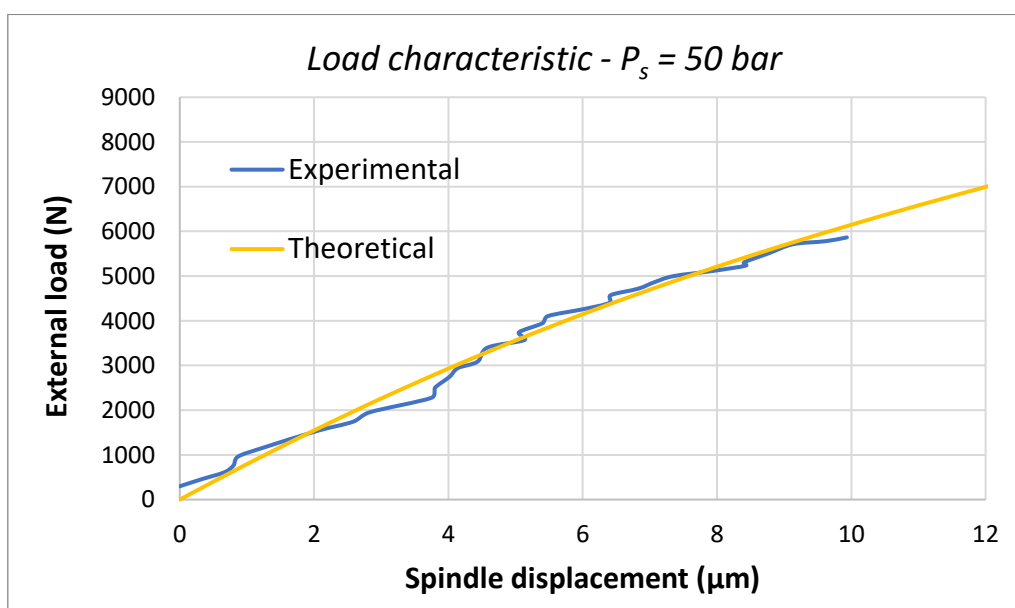


Figure 65. Hydrostatic spindle force-displacement relation between experimental and theoretical behavior. $P_s = 50$ bar, $h_d = 15\mu\text{m}$.

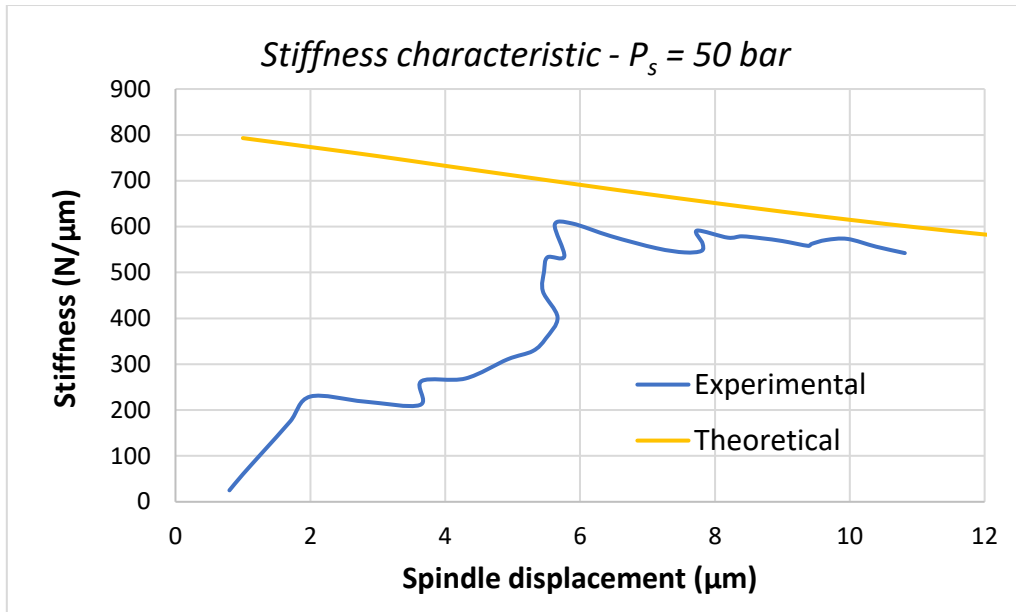


Figure 66. Hydrostatic spindle stiffness-displacement relation between experimental and theoretical behavior. $P_s = 50$ bar, $h_d = 15\mu\text{m}$.

Now, comparing the experimental behaviors of the system when the oil gap is 15 microns and when it is 30 microns to the theoretical ones with a supply pressure equal to 50 bar, it can be observed that in the case of 30 microns gap the curves do not fit – as said earlier due of pressure losses - while in the case of 15 microns gap, they do.

If we add to this that when the system has a gap of 15 microns and it is fed by a pressure of 30 bar, its experimental characteristics better represent the theoretical behavior, is possible to think that this discrepancy may be due to the fact that the 15 microns clearance has not been adjusted correctly. It is possible that the clearance given to the system is slightly increased - bigger than 15 microns and anyway smaller than 30 microns - so the system reacts better to external loads and this overestimate the experimental results.

This phenomenon can also be explained by considering the system flow rate when the supply pressure is 50 bar. For a system with 15 microns oil gap that operates at a supply pressure of 50 bar the total flow rate is about $0,82\text{ l/min}$. On the other hand, the flow rate calculated under the same conditions is approximately 1 l/min , therefore this confirms the difference between experimental and theoretical oil film thickness.

4.3 Results overview

Beside the problematics, the experimental results show a good correlation with the theoretical ones. In the vast majority of tests, experimental curves show the same angular coefficient of the theoretical but with a different offset of the curve. In reality, if we focus on figure 67, the left side of the graph shows oscillations, and there is a jump at around 4-5 microns of the spindle displacement, letting the experimental data not match the theoretical ones.

The problem here is the resolution of the measuring instrument and/or the compensation process of measuring. Anyway, each process has been measured through the same instrument, the millesimal dial indicator.

Observing the figure 67, it is possible to notice that, beside the oscillations, the 30-bar test correctly represents the behavior of the system. Increasing the supply pressure, the trend of the experimental curves worsens, especially the angular coefficient.

The graph clarifies the already discussed problematics of the system.

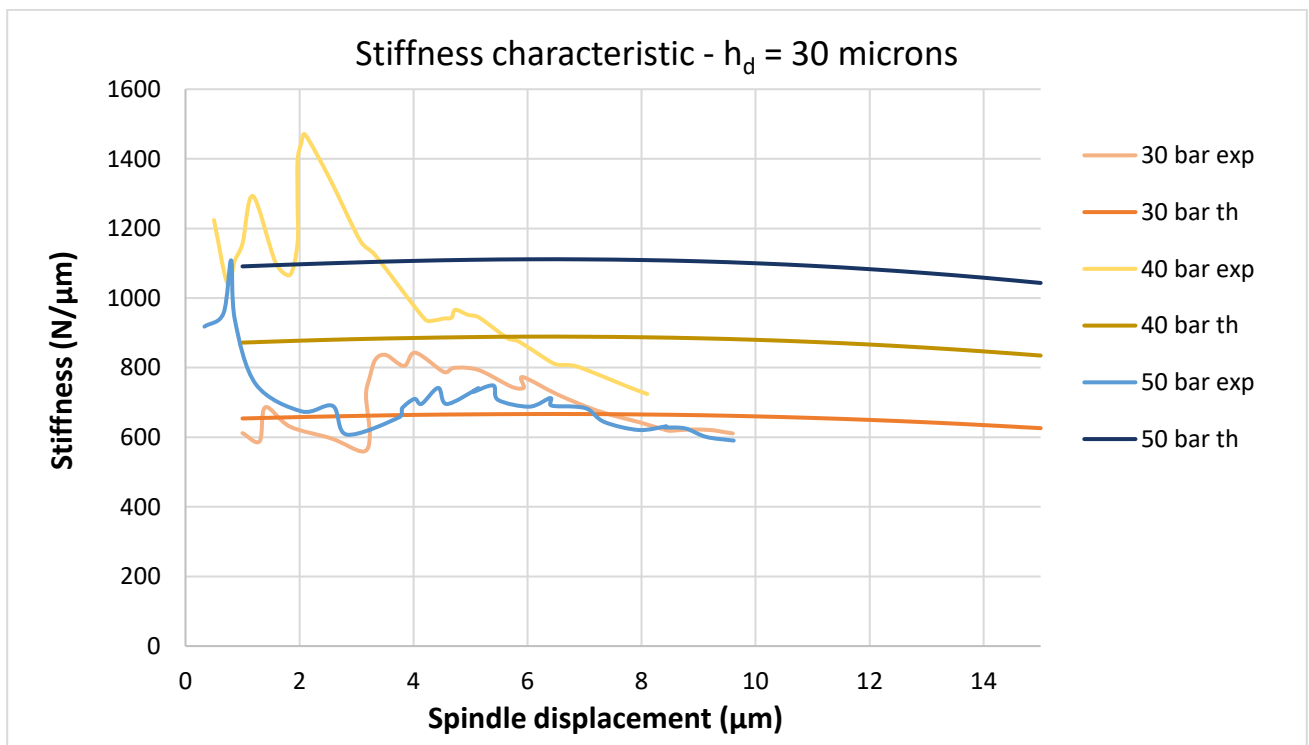


Figure 67. Stiffness comparison of the system between three different pressure with oil gap of 30 microns.

The main test was made passing from 30 microns oil gap to 15 microns oil gap, but to verify that the behavior of the real system matches the behavior of the project, another test changing the oil film thickness was carried out. The performance of the system is consistent with the project.

Figure 68 and figure 69 confirm that the behavior of the system is completely coherent with that designed. Basically, the best stiffness of the system is obtained when the oil film thickness is pair to 30 microns; from there all others oil thickness values guarantee a lower stiffness. Particularly, halving it we obtain a better behavior than duplicating it, as the theoretical data show.

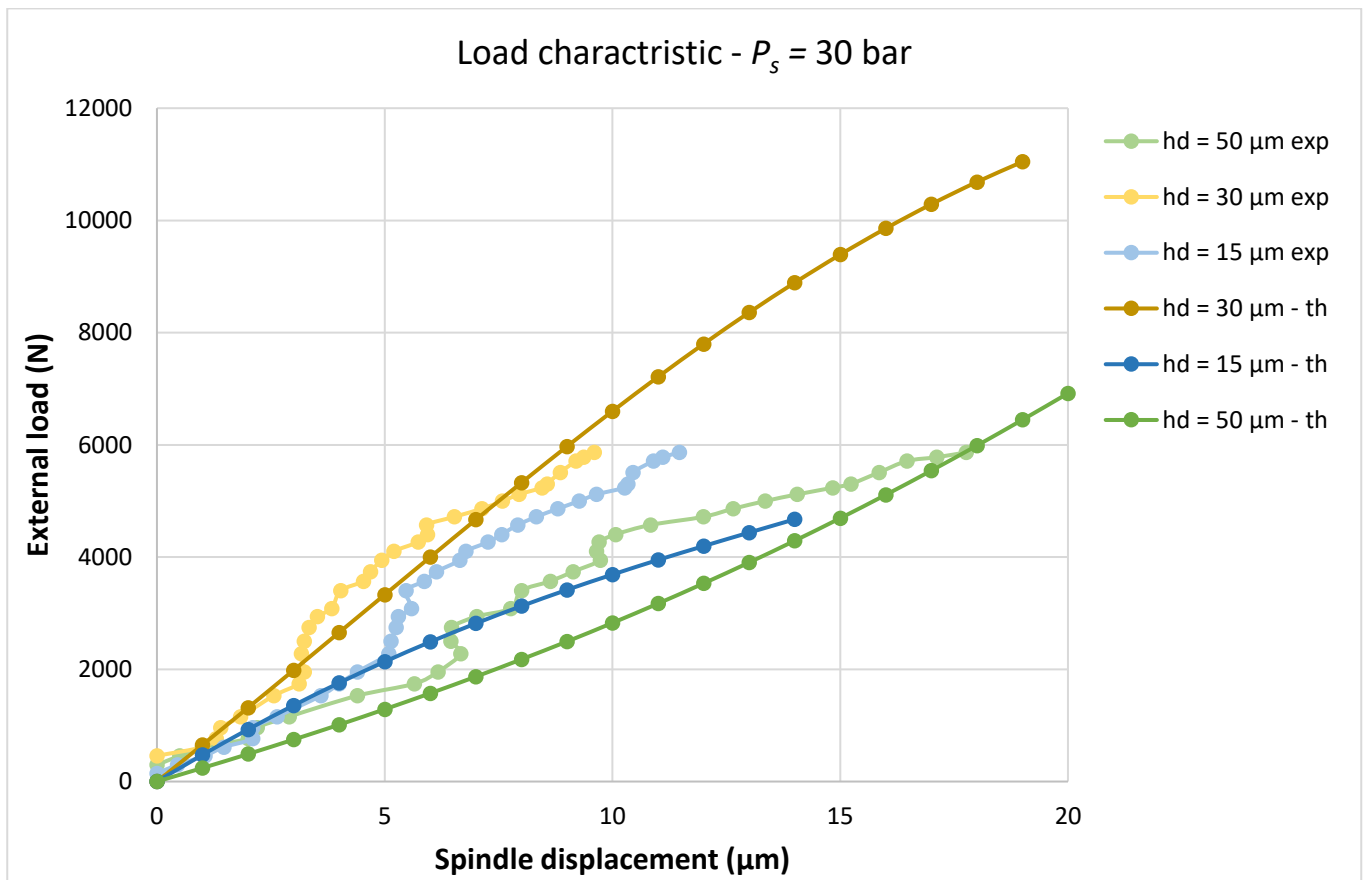


Figure 68. Comparison of load characteristic by varying the clearance of the system. $P_s = 30$ bar.

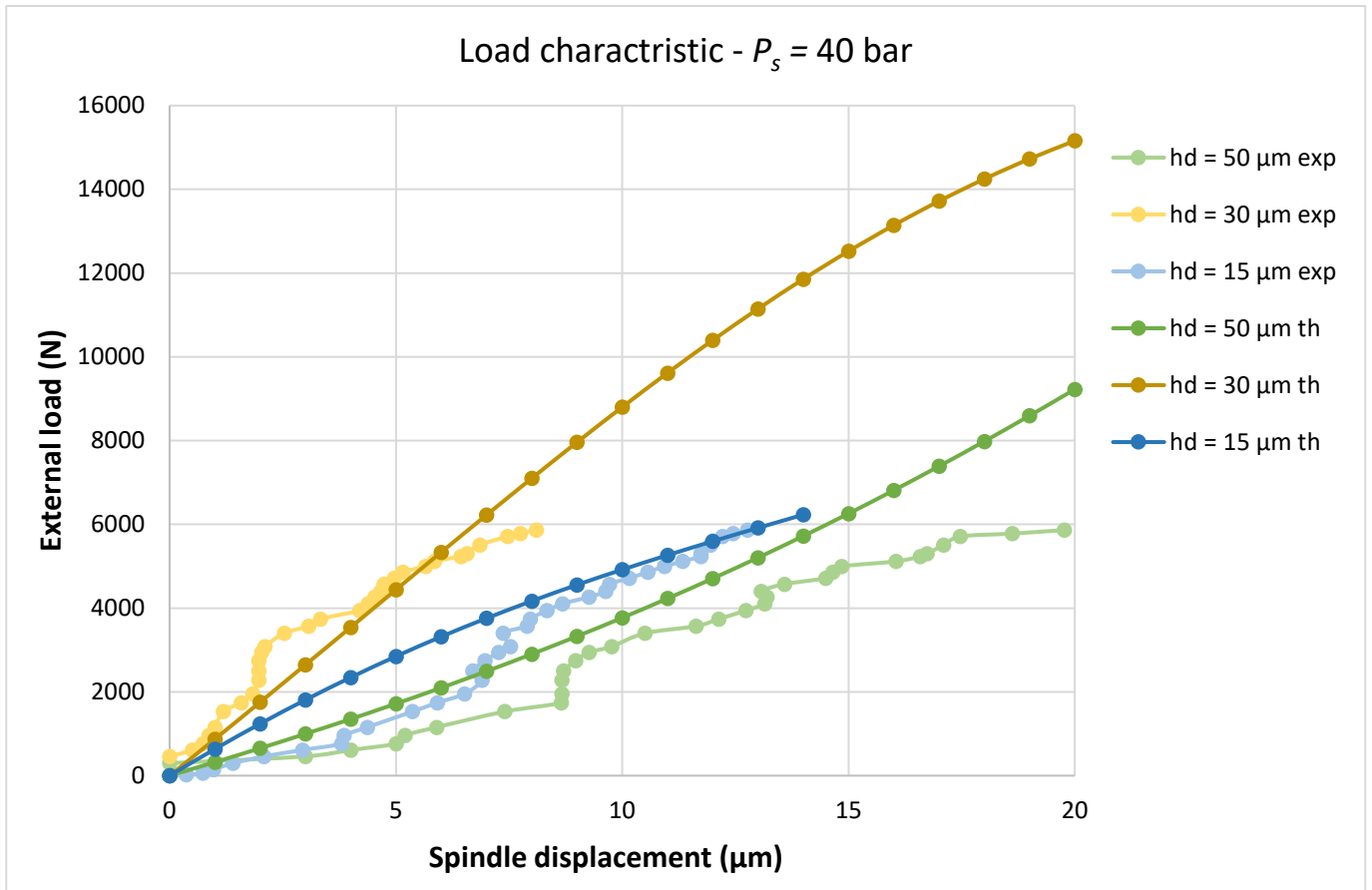


Figure 69. Comparison of load characteristic by varying the clearance of the system. $P_s = 40$ bar.

The last two showed graphs demonstrate the coherence of the realized system to the designed one and, beyond the issues encountered, the system performs reasonably well at 30 and 40 bar of the pressure supply.

Conclusions

The research stems from the need to find reliable solutions in the field of centerless grinding operations, as the current hydrodynamic technologies used by the company “Bocca & Malandrone S.r.l.” are limiting. The aim of the research is to characterize the behavior of a hydrostatic system that allows better performances than the actual machinery.

The procedures used to implement the system under studying are divided in five sections: research, design, elements realization, assembly, and test.

Being a very specialistic topic, several hours were spent researching the appropriate documentation to best understand the mechanism. The design process was carried out taking into account the load and stiffness characteristic we wanted to achieve in mind. In any case, the characteristics of the designed machine go far beyond the real application, but we wanted to study what was the reliability of the system for higher performances.

The fabrication of each individual part was done in-house, and this facilitated the process because of the immediate communication between the designer and the machine tool operator. In addition, when there were design errors, the fabrication of a new part was immediate. The next step was the assembly of the system, which was expedited with the help of some members of the company.

Finally, experimental tests are performed to characterize the behavior of the system and compare the data with theoretical data.

To evaluate the stiffness of the system, a system capable of generating an external load on the spindle is constructed, thus causing a displacement of the spindle. Then, measuring the displacement and knowing the force applied on the spindle, it is possible to go back to the load and stiffness characteristic.

It is built an electromagnet that, thanks to the current it receives, is able to attract the spindle towards itself. A dial gauge is used to record the displacement of the shaft. By varying the current, different loads are generated on the shaft and the relative displacements are measured. Load and stiffness characteristics are constructed for different feed pressures and different oil film thickness.

Overall, the results obtained reflect those of the project, but several limitations of the realized system become apparent. The tests conducted at lower pressures roughly reflect the theoretical behavior of the system, while the tests at 50 bar, which represents the design supply pressure, are not very consistent with the design.

The discrepancies between theoretical and experimental are due to the following problems that were found:

- bushings asymmetry,
- inaccurate clearance setting,
- uncomfortable and inaccurate magnet loader air gap adjustment,
- pressure losses due to complex connection system,
- inadequate measuring instrument.

Bushing asymmetry is caused by incorrect material processing. The difference in width between the lands and the asymmetry of the hole on which the part is clamped are the main problem of the inefficiency of the system. This imperfection on the pads causes uneven pressure distribution which creates leaks through the pads, thus decreasing stiffness.

The clearance is adjusted by rotating a threaded strut. Since the screw pitch is up to two orders of magnitude larger than the desired clearance, this results in an inaccuracy in adjustment, especially when very small clearance is desired.

Regarding the magnetic loader, the air gap between the electromagnet and the spindle is a very sensitive parameter and to allow the tool to function properly, the air gap must be uniform across the diameter. For this purpose, flexible shims were used. The problem is that this method of adjustment is coarse and results in an inhomogeneity of the air gap, worsening the performance of the device.

The connections of the elements that bring the oil to the bushings were not extremely reliable. The mechanism for connecting the tubes is limiting and complex. In order to connect the tubes to the stopper and the bushings, it is necessary to first insert the O-ring, then crush it by screwing in the grub screw and finally insert the tube by tapping it with a hammer, risking bending it.

In addition, you must not turn the screw too much, otherwise the O-ring will be crushed too much, and the tube will not enter, and you must not screw it in too little, otherwise it will leak. It is a complex process that took a lot of time and moreover it is not possible to evaluate the correctness of the assembly because when everything is assembled you cannot see what happens inside.

Last but not least, the measuring instrument used is not extremely accurate for this application.

Since the spindle moves radially by a few tens of microns, and the measuring instrument has a resolution on the order of microns, accuracy in recording small displacements is lost. In fact, it can be seen that all tests have noticeable oscillations for small spindle displacements.

The system is very limited but with the appropriate corrections a very high level of reliability can be achieved.

The first step is to make the bushings correctly, perhaps using a numerically controlled machine instead of a traditional one, and to find a more reliable system for adjusting the clearance or to create a machine that guarantees a fixed but accurate clearance.

It is advisable to think of a simpler and more reliable distribution system, for example it is possible to increase the diameter of the tubes and make connections with ogive fittings. It would also be advisable to design the system in such a way as to visualize what is happening between the bushings and the spindle, and possibly place pressure sensors for greater control of the system.

The use of displacement sensors and load cells would allow refinement of the achievable results. Finally, improve the mounting of the magnet loader or use a more reliable alternative system.

In conclusion, despite the difficulties and problems encountered, the results obtained can be considered appropriate.

Appendix A

Table 21. Designed parameters for the two kind of bearing pads.

		Smaller Pad	Bigger Pad	
Spindle radius	Rm	28,00	35,00	mm
Length capillary tube	lc	100,00	100,00	mm
Diameter capillary tube	dc	0,70	0,70	mm
Length	L	78,50	106,00	mm
Width	B	38,16	47,69	mm
Land width	C _x	8,02	7,95	mm
	C _y	8,02	23,23	mm
Recess depth	H	0,50	0,50	mm
Internal pad radius	r _p	28,03	35,03	mm
Effective area	Av	2059,50	3104,54	mm ²
Arc of the circle		78,00		°
		1,36		rad
Design pressure ratio	β	0,53	0,51	
Precess design	Pr design	26,58	25,69	bar
Supply pressure	Ps	50,00	50,00	bar
Inflow resistance	Ri	3,00E+11	3,00E+11	kg/sm ⁴
Outflow resistance	Ro	3,35E+11	3,12E+11	kg/sm ⁴
Design film thickness	h ₀	0,03	0,03	mm
Total lubricant flow	Q	23,30	24,18	cm ³ /s
Design load capacity	Wd	5468,00	8353,00	N
Hydrostatic stiffness	λ _{hs}	512,32	812,13	N/μm
Spindle mass	m	20,00		kg
Damping squeeze	Csq	0,58	1,57	Ns/μm
Natural frequency	ω _n	701,33	1014,14	Hz
Damping ratio	ξ	3,32	6,14	
Maximum pad deflection		5,39	14,98	μm

Appendix B

Table 22. Mitutoya micrometric feeler gauger datasheet.

Accuracy [μm]	± 2
Resolution [μm]	1
Measuring range [mm]	0-25
Weight [g]	175

Table 23. Correlation between current, electromagnetic force, spindle displacement and stiffness for the system with 30 microns oil film thickness for a pressure supply of 30, 40 and 50 bar.

Magnet loader		Design film thickness 30 μm					
		50 bar		40 bar		30 bar	
Current (A)	External force (N)	Spindle displacement (μm)	Spindle stiffness (N/ μm)	Spindle displacement (μm)	Spindle stiffness (N/ μm)	Spindle displacement (μm)	Spindle stiffness (N/ μm)
0,5	0						
0,6	20						
0,7	60						
0,8	142						
0,9	298	0,0					
1	459	0,3	1377	0,0		0,0	
1,1	612	0,7	918	0,5	1224	1,0	612
1,2	765	0,8	956	0,7	1043	1,3	588
1,3	961	0,9	1108	0,9	1108	1,4	686
1,4	1156	1,2	937	1,0	1156	1,8	631
1,5	1530	2,0	752	1,2	1293	2,6	596
1,6	1743	2,6	675	1,6	1101	3,1	559
1,7	1955	2,8	690	1,8	1066	3,2	605
1,8	2278	3,8	607	2,0	1158	3,2	719
1,9	2499	3,8	658	2,0	1271	3,2	773
2	2746	4,0	684	2,0	1396	3,3	824
2,1	2941	4,1	710	2,0	1446	3,5	836
2,2	3086	4,4	696	2,1	1469	3,8	805
2,3	3400	4,6	742	2,5	1342	4,0	843
2,4	3570	5,1	695	3,1	1164	4,5	788
2,5	3740	5,1	741	3,3	1122	4,7	799
2,6	3944	5,4	730	4,2	939	4,9	799
2,7	4106	5,5	749	4,4	937	5,2	790
2,8	4267	6,0	707	4,5	941	5,7	744
2,9	4403	6,4	688	4,7	944	5,9	742
3	4573	6,4	713	4,7	966	5,9	773
3,1	4718	6,8	691	5,0	951	6,5	723
3,2	4862	7,1	688	5,2	944	7,1	682
3,3	4998	7,4	680	5,7	885	7,6	659
3,4	5117	8,0	644	5,9	875	8,0	644
3,5	5236	8,4	621	6,4	814	8,5	620
3,6	5304	8,4	631	6,6	808	8,6	619
3,7	5508	8,8	628	6,9	804	8,9	622
3,8	5712	9,1	625	7,5	765	9,2	621
3,9	5780	9,6	601	7,8	746	9,4	617
4	5865	9,9	590	8,1	724	9,6	611

Table 24. Correlation between current, electromagnetic force, spindle displacement and stiffness for the system with 15 microns oil film thickness for a pressure supply of 30, 40 and 50 bar.

Magnet loader		Design film thickness 15 μm					
		50 bar		40 bar		30 bar	
Current (A)	External force (N)	Spindle displacement (μm)	Spindle stiffness (N/ μm)	Spindle displacement (μm)	Spindle stiffness (N/ μm)	Spindle displacement (μm)	Spindle stiffness (N/ μm)
0,5	0	0,6		0,0			
0,6	20	0,8	25	0,4	55		
0,7	60	1,0	60	0,7	82		
0,8	142	1,3	109	1,0	147	0,0	
0,9	298	1,7	175	1,4	213	0,5	661
1	459	2,0	230	2,1	220	1,1	437
1,1	612	2,8	219	2,9	209	1,5	417
1,2	765	3,6	211	3,8	201	2,1	364
1,3	961	3,7	263	3,9	249	2,1	457
1,4	1156	4,3	269	4,4	265	2,6	439
1,5	1530	4,9	311	5,4	285	3,6	425
1,6	1743	5,3	329	5,9	295	4,0	436
1,7	1955	5,5	356	6,5	300	4,4	444
1,8	2278	5,7	402	6,9	330	5,1	448
1,9	2499	5,5	459	6,7	373	5,1	487
2	2746	5,5	502	7,0	394	5,3	523
2,1	2941	5,5	533	7,3	405	5,3	555
2,2	3086	5,8	535	7,5	410	5,6	553
2,3	3400	5,6	604	7,4	462	5,5	622
2,4	3570	5,9	607	7,9	452	5,9	609
2,5	3740	6,5	579	8,0	469	6,1	610
2,6	3944	7,1	553	8,3	473	6,7	593
2,7	4106	7,6	544	8,7	473	6,8	605
2,8	4267	7,8	547	9,3	460	7,3	587
2,9	4403	7,8	563	9,6	457	7,6	582
3	4573	7,7	591	9,7	471	7,9	578
3,1	4718	8,2	576	10,2	464	8,3	567
3,2	4862	8,4	579	10,6	460	8,8	553
3,3	4998	8,7	574	10,9	457	9,3	539
3,4	5117	9,0	569	11,3	452	9,7	530
3,5	5236	9,4	558	11,7	446	10,3	510
3,6	5304	9,4	562	11,7	452	10,3	513
3,7	5508	9,7	571	12,0	461	10,5	527
3,8	5712	10,0	573	12,2	468	10,9	524
3,9	5780	10,4	556	12,5	464	11,1	521
4	5865	10,8	542	12,8	459	11,5	511

Appendix C



Figure 70. Step 1 – Putting the bushing on the engineering blue on the spindle.

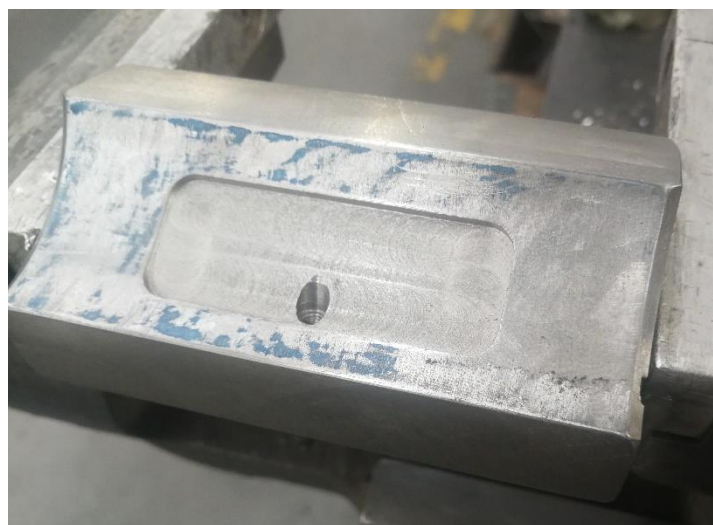


Figure 71. Step 2 – Evaluation of blue points and getting ready to scrape them.



Figure 72. Step 3 - Scraping process.



Figure 73. Final result of scraped pads.

Bibliography

- [1] Hua-Chih Huang, Ching-Yuan Lin, Farid Al-Bender, *Design Analysis of Recess-Type Hydrostatic Slide Systems*. Katholieke Universiteit Leuven – Leuven, Belgium.
- [2] W. B. Rowe, *Hydrostatic and Hybrid Bearing Design*. London: Butterworths, 1983.
- [3] Antony Raymond Wong, *Design of low cost hydrostatic*. Massachusetts Institute of Technology, 2012.
- [4] W. B. Rowe, *Hydrostatic, Aerostatic and Hybrid Bearing Design*. Oxford: Butterworths, 2012.
- [5] Alexander H. Slocum, *Water hydrostatic bearing for precision machine tools and industrial machinery*. Massachusetts Institute of Technology – Cambridge, MA, USA 02139.
- [6] W.B. Rowe, *Advances in hydrostatic and hybrid bearing technology*. School of Engineering and Technology Management, Liverpool Polytechnic. IMechE, 1989.
- [7] Taku Yamazaki, *Measurement of Spindle Rigidity by using a Magnet Loader*. Product Development Department, Yamazaki Mazak Corporation, Oguchi-cho, Aichi 480-0197, Japan, 2010.
- [8] Xiaopeng Wang, Yuzhu Guo, and Tianning Chen, *Measurement Research of Motorized Spindle Dynamic Stiffness under High Speed Rotating*, School of Mechanical Engineering, State Key Laboratory for Strength and Vibration of Mechanical Structures, Xi'an Jiaotong University, Xi'an 710049, China, 2015.
- [9] Sorli M., Quaglia G., *Meccatronica vol.1*. Politeko, Torino, 2003.
- [10] EN 1562 Grade GJMW-350-4 decarburized annealed—Published on “Matmatch” website, <https://matmatch.com/>
- [11] A.W. Kwiatkowski, *A magnetic vibrator for the determination of machine tool dynamic characteristics*, in *proceedings of the 9th MTDR Conference*, vol. 1, pp. 571–590, Pergamon Press, Oxford, UK, 1968.
- [12] Hélio F. de Castro, Rogério M. Furtado, Katia L. Cavalca, Robson Pederiva, Norman Butzek, Rainer Nordmann, *Experimental Performance Evaluation of Magnetic Actuator used in Rotating Machinery Analysis*, *Journal of the Brazilian Society of Mechanical Sciences and Engineering*, Vol. XXIX, No. 1, ABCM, 2007.